Congenital disorder of glycosylation caused by starting site-specific variant in syntaxin-5

Peter T.A. Linders[1], Eveline C.F. Gerretsen[1], Angel Ashikov[2,3], Mari-Anne Vals[4,5], Rinse de Boer[6], Natalia H. Revelo[1], Richard Arts[1], Melissa Baerenfaenger[2], Fokje Zijlstra[3], Karin Huijben[3], Kimiyo Raymond[7], Kai Muru[5,8], Olga Fjodorova[8], Sander Pajusalu[5,8], Katrin Õunap[5,8], Martin ter Beest[1], Dirk Lefeber[2,3,*] and Geert van den Bogaart[1,9,*]

[1] Department of Tumor Immunology, Radboud Institute for Molecular Life Sciences, Radboud University Medical Center, 6525 GA Nijmegen, The Netherlands

[2] Department of Neurology, Donders Institute for Brain, Cognition and Behavior, Radboud University Medical Center, 6525 GA, Nijmegen, The Netherlands

[3] Translational Metabolic Laboratory, Department of Laboratory Medicine, Radboud University Medical Center, 6525 GA, Nijmegen, The Netherlands

[4] Children's Clinic, Tartu University Hospital, Estonia

[5] Department of Clinical Genetics, Institute of Clinical Medicine, University of Tartu, Estonia

[6] Molecular Cell Biology, Groningen Biomolecular Sciences and Biotechnology Institute, University of Groningen, Groningen, The Netherlands

[7] Department of Laboratory Medicine and Pathology, Mayo College of Medicine, Rochester, Minnesota, USA.

[8] Department of Clinical Genetics, United Laboratories, Tartu University Hospital, Tartu, Estonia

[9] Department of Molecular Immunology, Groningen Biomolecular Sciences and Biotechnology Institute, University of Groningen, 9747AG, Groningen, Netherlands

[*] Correspondence: dirk.lefeber@radboudumc.nl; Tel.: +31-24-36-14567; g.van.den.bogaart@rug.nl; Tel.: +31-50-36-35230

Abstract

The SNARE (soluble N-ethylmaleimide-sensitive factor attachment protein receptor) protein syntaxin-5 (Stx5) is essential for Golgi transport. In humans, the *STX5* mRNA encodes two protein isoforms, Stx5 Long (Stx5L) from the first starting methionine and Stx5 Short (Stx5S) from an alternative starting methionine at position 55. In this study, we identify a human disorder caused by a single missense substitution in the second starting

methionine (p.M55V), resulting in complete loss of the short isoform. Patients suffer from an early fatal multisystem disease, including severe liver disease, skeletal abnormalities and abnormal glycosylation. Primary human dermal fibroblasts isolated from these patients show defective glycosylation, altered Golgi morphology as measured by electron microscopy, mislocalization of glycosyltransferases, and compromised ER-Golgi trafficking. Measurements of cognate binding SNAREs, based on biotin-synchronizable forms of Stx5 (the RUSH system) and Förster resonance energy transfer (FRET), revealed that the short isoform of Stx5 is essential for intra-Golgi transport. Alternative starting codons of Stx5 are thus linked to human disease, demonstrating that the site of translation initiation is an important new layer of regulating protein trafficking.

Keywords

Syntaxin-5, ER-Golgi trafficking, glycosylation, secretory pathway, congenital disorders of glycosylation

42 **Introduction**

43 In eukaryotes, proteins destined for the secretory pathway are synthesized at the endoplasmic reticulum (ER)
44 and then transported to the Golgi apparatus, where they are sorted for their ultimate destinations at the
45 trans-Golgi network. Central to this process is intracellular membrane fusion, which is mediated by members
46 of the SNARE (soluble N-ethylmaleimide-sensitive factor attachment protein receptor) protein family. Cognate
47 SNARE proteins that are present in both the carrier vesicle and target membranes, called v- and t-SNAREs
48 respectively, engage and form a tight alpha-helical coiled-coil bundle that overcomes the energy barrier of
49 membrane fusion. Membrane fusion requires a single R-SNARE, characterized by an arginine residue located
50 central in the SNARE bundle, and three Q-SNAREs, with glutamine residues instead. Generally in mammalian
51 cells, the R-SNAREs act as vesicle (v-) SNAREs and the Q-SNAREs together form the t-SNARE complex on the
52 target membrane[1]. In contrast, the Qc-SNAREs Bet1 and Bet1L (GS15) function as the v-SNAREs at the ER/Golgi
53 interface[2–5], while, for anterograde ER to Golgi trafficking, the recipient t-SNARE complex is formed by the Qa-
54 SNARE syntaxin-5 (Stx5)[6–9], together with the Qb-SNAREs GosR1 (also known as GS27 or membrin) or GosR2
55 (GS28), and R-SNAREs Ykt6 or Sec22b (Ers24)[10–12]. This different allocation of the Qc-SNAREs Bet1 and Bet1L as
56 v-SNARE instead of t-SNARE possibly prevents the formation of non-functional SNARE complexes during ER to
57 Golgi transit. In addition, Stx5 functions in retrograde intra-Golgi transport by forming a recipient t-SNARE
58 complex with GosR1, and Ykt6[5,13] and in retrograde trafficking from endosomes to the trans-Golgi network
59 (TGN)[14,15], making it a unique SNARE protein involved in both anterograde and retrograde Golgi transport.

60 *STX5* is highly conserved and is an essential gene in animals and fungi[16,17]. In animals, Stx5 exists as a long and
61 a short isoform translated from the same mRNA: 39.6 kDa sized Stx5 Long (Stx5L) and 34.1 kDa sized Stx5
62 Short (Stx5S)[13,18]. This is in contrast to lower organisms, such as *Saccharomyces cerevisiae*, which only express
63 a single isoform of Stx5 (Sed5p). Although Sed5p was originally believed to resemble mammalian Stx5S[13], it is
64 now clear that it likely more resembles Stx5L, since an N-terminal COPI-binding tribasic motif has been
65 identified in Sed5p[19]. The emergence of a second Stx5 isoform can be traced back to the pacific purple sea
66 urchin, *Strongylocentrotus purpuratus*, and is also present in the model organism *Danio rerio*, but not in
67 *Drosophila melanogaster* nor *Caenorhabditis elegans*. Compared to Stx5S, Stx5L contains 54 extra N-terminal
68 residues bearing an Arginine – Lysine – Arginine (RKR) ER retrieval motif, and as a result, Stx5L locates more to
69 the ER whereas Stx5S locates more to the Golgi network[13,18,20–22]. The evolutionary necessity of the two Stx5
70 isoforms remains unclear but it has been suggested that Stx5L is important to maintain ER structure by binding

71 microtubules, possibly via CLIMP-63[21,23]. In addition, immunoprecipitations showed that GosR1 and Bet1L
72 preferentially interact with Stx5S over Stx5L[24,25], suggesting that Stx5S might act in more fusogenic complexes
73 later at the ER-Golgi interface whereas Stx5L might be more involved in earlier fusion steps.
74 In the present study, we identified a genetic variant in the second translation codon methionine-55, fully
75 abrogating the production of Stx5S and providing an opportunity to study the physiological relevance of the
76 existence of two isoforms in humans. Patients homozygous for this mutation have a severe clinical phenotype
77 associated with infantile mortality and defective protein glycosylation. We demonstrate that although Stx5L
78 can largely compensate for the lack of Stx5S, the loss of Stx5S leads to defects in intra-Golgi trafficking with
79 altered morphology of the ER and Golgi apparatus and mislocalization of glycosyltransferases, which results in
80 pronounced defects in glycosylation. Moreover, by synchronizing the intracellular trafficking of Stx5 isoforms
81 and Förster resonance energy transfer microscopy (FRET) coupled to fluorescence lifetime imaging microscopy
82 (FLIM), we reveal differential SNARE interactions for either isoform and identify Stx5S as the dominant Qa-
83 SNARE for intra-Golgi transport. A mutation in an alternate starting site of ribosomal translation of Stx5 is thus
84 linked to human disease. This finding reveals that protein function can be regulated at the level of translation
85 initiation and has profound effects on intracellular membrane trafficking and Golgi function.
86
87 **Results**
88 ***Clinical data***
89 The family history (Supplementary Fig. 1) revealed multiple deceased individuals (IV:3, IV:9, IV:10) shortly after
90 birth, spontaneous abortions (IV:5, IV:6, IV:7), and elective abortions during pregnancy due to abnormal fetal
91 ultrasound (US) (IV:4, IV:8). Fetal US of individuals IV:8, IV:9, and IV:10 showed shortening of the long bones
92 with suspicion of chondrodysplasia. Patients IV:9 and IV:10 showed highly dysmorphic facial features (high
93 forehead, frontal bossing, prominent glabella, short and upturned nose, long philtrum, micrognathia and
94 dysplastic ears), skeletal dysplasia (short extremities and narrow thorax), profound hypotonia, hepatomegaly,
95 and many abnormal laboratory parameters including elevated cholesterol (Supplementary Table 1). After
96 birth, the main clinical problem for both patients IV:9 and IV:10 was progressive liver failure with cholestasis
97 and hyperinsulinemic hypoglycemia (Supplementary Table 1). Liver failure was the main cause of death at the
98 age of 0-3 months and 6-9 months, in patients IV:9 and IV:10, respectively. Autopsy of fetus IV:8 revealed
99 bilateral hydronephrosis and sacral lordosis. Autopsy of patient IV:9 showed hepatomegaly with stage 3 to 4

100 liver fibrosis, agenesis of left kidney, hyperemia of internal organs, ventricular septal defect and suggestive
101 pathohistological features of chondrodysplasia. Autopsy of patient IV:10 showed biliary cirrhosis and nodular
102 regenerative hyperplasia, pancreatic hypertrophia/hyperplasia, and narrow thorax with normal lung
103 development.
104
105 ***Abnormal protein glycosylation suggests a defect in Golgi trafficking***
106 Known genetic causes for skeletal dysplasias were excluded (IV:8), no submicroscopic chromosomal
107 abnormalities were found, while most metabolic investigations were normal except for the Congenital
108 Disorders of Glycosylation (CDG) (IV:9 and IV:10). CDG screening revealed a strong hyposialylation of protein
109 N-glycosylation and mucin-type O-glycosylation, as analyzed by isofocusing of respectively plasma transferrin
110 (Fig. 1a, Supplementary Table 2) and apolipoprotein CIII (ApoCIII-IEF, Fig. 1b, Supplementary Table 2). ApoCIII-
111 IEF showed a strong increase of non-sialylated apoCIII (ApoCIII-0) band intensities compared to the intensities
112 of the fully glycosylated form, even stronger than observed for genetic defects in the Conserved Oligomeric
113 Golgi (COG) complex, a known group of disorders with disturbed Golgi homeostasis and abnormal
114 glycosylation[26].
115 To gain more insight into the abnormal N-glycan structures, mass spectrometry was performed of intact
116 transferrin (Fig. 1c, d, Supplementary Fig. 2) and of total plasma protein derived N-glycans (Fig. 1c, e,
117 Supplementary Fig. 3). Analysis of intact transferrin of individuals IV:9 and IV:10 revealed multiple abnormal
118 glycan structures, divided into two categories: high mannose structures and truncated glycans. Compared to
119 the peak height of completely glycosylated transferrin, a dominant accumulation was found of high-mannose
120 glycans (Supplementary Table 3, Man5, mass/peak number) suggesting a problem with MGAT1, the enzyme
121 that adds the next N-acetylglucosamine during N-glycosylation. Furthermore, a series of transferrin isoforms
122 was observed with reduced incorporation of galactose and sialic acid residues. Similar glycosylation patterns
123 were observed in COG5-CDG[27–30]. Analysis of N-glycans released from total plasma proteins recapitulated the
124 two categories of abnormal glycans with the accumulation of high mannose glycans, as well as reduced
125 incorporation of galactose and sialic acid residues (Supplementary Table 4). Together, these data indicate that
126 the activities of multiple glycosyltransferases in the Golgi apparatus are affected, covering both N- and O-
127 glycosylation, thereby suggesting a general disturbance in Golgi trafficking.
128

129 ***Molecular investigations result in the identification of variants in STX5***

130 Chromosomal microarray analysis (CMA) using HumanCytoSNP-12 microarrays revealed multiple long
131 contiguous stretches of homozygosity (LCSH, >5 Mb) distributed across the entire genome, with several
132 regions of homozygosity on chromosome 11 in all three affected sibs (IV:8, IV:9 and IV:10, Supplementary
133 Table 5). Exome sequencing was performed in proband IV:9 to find the genetic variant that could be associated
134 with the disease. Only two homozygous rare protein-altering variants without homozygous individuals in the
135 gnomAD v3 database were identified in shared homozygous stretches on chromosome 11. First, a missense
136 variant in the *VPS37C* gene was discovered (NM_017966.4:c.760G>T p.(Gly254Cys) rs201088253). However, as
137 this variant reaches an allele frequency of 0.9% in Estonia, it is unlikely to cause a rare genetic disorder. The
138 second variant was identified in the *STX5* gene (NM_003164.4:c.163A>G p.(Met55Val), Fig 2a). This is a
139 missense mutation affecting the alternative starting codon for the production of the short Stx5 isoform. The
140 variant is absent from the gnomAD v3 database and was thus classified as a potentially disease-causing
141 variant. The variant was confirmed by Sanger sequencing as homozygous in all affected individuals (IV:8, IV:9,
142 and IV:10) and as heterozygous in the mother (III:2). Paternal DNA was not available for testing.

143 To confirm the effect of the genetic variant on both Stx5 proteoforms, immunoblotting was performed in
144 primary dermal fibroblasts of patients IV:9 and IV:10. While Stx5L was present, a total absence of Stx5S was
145 found in both patient fibroblasts (Fig. 2b, c). We next tested the expression of known interaction partners of
146 Stx5. The levels of Qc-SNARE Bet1L, which forms a complex with Stx5 upon retrograde intra-Golgi
147 trafficking[5,13–15], were also reduced. In contrast, the expression of Qc-SNARE Bet1, which forms a complex with
148 Stx5 upon anterograde ER-Golgi trafficking[10,12,13,31] was not reduced (Fig. 2b, c). Likewise, the expression of Qb-
149 SNAREs GosR1 and GosR2, which can complex with Stx5 for anterograde ER-Golgi trafficking and retrograde
150 intra-Golgi trafficking[5,9,10,12,13,24] were unaltered in patient dermal fibroblast lysates. We hypothesized that a
151 compensatory mechanism might exist by upregulating the expression of the trans-Golgi Qa-SNARE Stx16[32],
152 usually involved in endosome-to-TGN trafficking[33], but we did not detect a change of Stx16 expression in
153 patient fibroblast lysates (Fig. 2b, c). As a first step to confirm that fibroblasts offer a useful model to
154 recapitulate the cell biological abnormalities due to loss of the Stx5S isoform, we studied glycosylation by
155 fluorescently-labeled lectins.

156

157 ***Glycosylation defects in Stx5M55V patient fibroblasts***

158 Patient fibroblasts could be cultured normally and we did not observe apparent differences in growth rate or
159 viability between healthy control and patient-derived cell lines. Cell surface staining with the lectin SNA-I from
160 *Sambucus nigra,* which binds terminal sialic acid in an α-2,6 linkage of fully-formed N-glycan moieties and, to a
161 lesser extent, sialic acid in an α-2,3 linkage, showed that glycosylation was also impaired at the cellular level in
162 patient fibroblasts. Compared to fibroblasts of healthy donors, we observed a more than two-fold reduced
163 SNA-I labeling intensity in Stx5M55V patient fibroblasts (Fig. 2d,e). Moreover, most signal came from
164 punctuated structures in the Stx5M55V patient fibroblasts, instead of the more uniform cell membrane
165 labeling observed in the healthy donor fibroblasts. To confirm this glycosylation defect, we performed cell
166 surface staining with the lectin PNA (Peanut agglutinin) from *Arachis hypogaea,* which binds terminal galactose
167 residues present on mucin O-glycan moieties of incompletely glycosylated proteins. Opposite to our findings
168 with SNA-I, we observed an increased labeling intensity in Stx5M55V patient fibroblasts relative to healthy
169 control by about six-fold (Fig. 2f,g). These findings show that patient-derived fibroblasts, which express Stx5L
170 but lack Stx5S, have a glycosylation defect.
171 Next, we evaluated the expression levels of Stx5S and Stx5L in lysates of peripheral blood mononuclear cells
172 (PBMCs) obtained from four different healthy donors (Supplementary Fig. 4). While total Stx5 expression levels
173 varied strongly (more than two-fold), the ratio of Stx5S and Stx5L was approximately equimolar for all
174 individuals, demonstrating that the expression ratio of the two isoforms is similar in PBMCs of different
175 healthy subjects.
176 To determine the role of Stx5S in Golgi transport, we generated a Stx5L-lacking fibroblast cell line from one of
177 the prior used control lines, using CRISPR/Cas9 (Fib Stx5ΔL, Supplementary Fig. 5a). We then performed the
178 same cell surface staining as described above. While we observed a similar decrease in SNA-I labeling intensity
179 in Stx5ΔL fibroblasts as in Stx5M55V patient fibroblasts, the staining pattern was more similar to healthy
180 control and showed a uniform plasma membrane-localized SNA-I labeling (Supplementary Fig. 5b-c). In
181 addition, opposite to Stx5M55V fibroblasts, the low PNA labeling intensity was reduced further in Fib Stx5ΔL
182 (Supplementary Fig. 5d-e). To investigate this difference further, we generated two clonal HeLa cell lines
183 lacking Stx5L using the same method (Stx5ΔL: B1A7 and C1F4, Supplementary Fig. 5f), and we observed a
184 decrease in the already low SNA-I labeling intensity as measured by FACS compared to the parental HeLa cells,
185 while PNA labeling resulted in opposite changes between the two Stx5ΔL lines (Supplementary Fig. 5g-k). The

186 difference in PNA labeling between the HeLa Stx5ΔL cell lines therefore likely is attributable by clonal variation
187 and/or off-target effects of CRISPR/Cas9. These results demonstrate that while the loss of Stx5S or Stx5L both
188 result in N-glycosylation defects, the defect is stronger upon the loss of Stx5S, as this results in lower levels and
189 a punctuated distribution of sialic acid moieties. Moreover, the mucin-type O-glycosylation defect seems
190 specific to the loss of Stx5S. As these results reiterate the glycosylation defect observed on serum transferrin,
191 total plasma N-glycans and apoCIII mucin O-glycans, patient fibroblasts are a suitable model to investigate the
192 cell biological consequences of the complete disruption of the Stx5S isoform.
193
194 ***Stx5M55V mutation results in mislocalization of glycosyltransferases***
195 Given that Stx5 mediates ER-Golgi trafficking[5,7,9–13,15,24,31], we next investigated whether the glycosylation
196 defect in Stx5M55V patient fibroblasts was caused by the mislocalization of glycosyltransferases. We
197 performed immunofluorescence labeling of mannosyl (α-1,3)-glycoprotein β-1,2-N-
198 acetylglucosaminyltransferase (MGAT1, also known as GnTI), which catalyzes the addition of GlcNAc to the
199 immature man-5 N-glycan. Compared to healthy donor fibroblasts, MGAT1 colocalizes only slightly less with
200 the cis-Golgi marker GM130 in patient fibroblasts (Fig. 3a, b), but colocalized substantially less with the trans-
201 Golgi network marker TGN46 (Fig. 3c, d). In addition, alpha-mannosidase 2 (MAN2A1), which catalyzes the
202 final hydrolytic step in the N-glycan maturation pathway after MGAT1 conversion, colocalized substantially less
203 with both GM130 (Supplementary Fig. 6a, b) and TGN46 in patient fibroblasts (Supplementary Fig. 6c, d).
204 Similarly to MGAT1, beta-galactoside alpha-2,6-sialyltransferase 1 (ST6GAL1), which catalyzes the transfer of
205 sialic acid to galactose residues of N-glycans in an α-2,6 linkage, colocalized less with both GM130
206 (Supplementary Fig. 6e, f) and TGN46 in patient fibroblasts (Supplementary Fig. 6g, h). Finally, N-
207 acetylgalactosaminyltransferase 2 (GALNT2), which catalyzes the initial reaction in mucin O-linked glycan
208 synthesis, localized more to the cis-Golgi (marker Zinc finger protein-like 1 (ZFPL1)[34]) (Fig. 3e, f) and less to the
209 trans-Golgi in patient fibroblasts (Fig. 3g, h).
210 To exclude the possibility that our conclusions were affected by potential mislocalization of TGN46 in the
211 patient cells, we repeated these experiments but now co-stained for another trans-Golgi marker, the trans-
212 Golgi coiled-coil protein p230[35] (Supplementary Fig. 7). Indeed, we observed similar Pearson correlation
213 coefficients for p230 as for TGN46 with MGAT1, GALNT2, MAN2A1, and ST6GAL1 (Supplementary Fig. 7).
214 Moreover, to confirm that the observed changes in colocalization were not due to lower expression of

215 glycosyltransferases, we performed immunoblotting for several glycosyltransferases and could not detect
216 consistent differences between control and Stx5M55V fibroblasts, although we noticed substantial variation in
217 protein expression levels of some of the glycosyltransferases between the samples (Supplementary Fig. 8),
218 reflecting expression differences among individuals and/or fibroblast lines.
219 Taken together, the loss of Stx5S results in irregular localization of glycosyltransferases to the Golgi apparatus.
220 An altered Golgi organization and mislocalization of glycosyltransferases can have a profound impact on
221 glycosylation as shown by computational simulations[36]. We investigated the organization of the Golgi complex
222 in Stx5M55V fibroblasts in more detail.
223
224 ***Loss of Stx5S alters the morphology of the ER and Golgi***
225 Transmission electron microscopy showed that the Golgi was not fragmented in the Stx5M55V patient
226 fibroblasts. However, we observed dilation of rough ER and Golgi cisternae in the Stx5M55V patient fibroblasts
227 (Fig. 4a-c, Supplementary Fig. 9), similar to previously observed alteration in the ultrastructure of the Golgi in
228 several COG defects[37–39]. Notwithstanding these large alterations in Golgi morphology, the polarized
229 arrangement of Golgi apparatus cisternae was still present in Stx5M55V, as observed by immunofluorescence
230 labeling of cis- and trans-Golgi markers (Supplementary Fig. 10). These results indicate that although Stx5L is
231 sufficient to maintain normal Golgi apparatus cisterna polarization, Stx5S is required for physiological ER and
232 Golgi ultrastructure and proper trafficking of glycosylation enzymes.
233 To address the role of the Stx5 isoforms in more detail, we studied the distribution of Stx5 isoforms in the
234 Golgi network. Because Stx5L contains an RKR ER-retrieval motif in its N-terminal extension, it locates more at
235 the ER compared to Stx5S[13,18,20,21]. In line with this, we observed a more dominant localization of Stx5L at the
236 ER and less at various Golgi compartments in Stx5M55V fibroblasts compared to total Stx5 localization in
237 healthy control fibroblasts (Supplementary Fig. 11a, b, d, e, Supplementary Fig. 12a, b, d, e).
238 A notable difference was the far more diffuse staining in Stx5M55V patients of the COPI coat protein βCOP
239 (Supplementary Fig. 11a, c) and of TGN46 (Supplementary Fig. 11d, f). In contrast, we observed a small
240 increase in GM130 fluorescence in Stx5M55V patients (Supplementary Fig. 12f). Since Western blot showed
241 that total cellular levels of βCOP and GM130 were not consistently altered in Stx5M55V patients
242 (Supplementary Fig. 11g), the more diffuse staining of βCOP is suggestive of reduced association with COPI-
243 coated vesicles, while the higher staining intensity of GM130 suggests more association with the cis-Golgi. In

244 contrast, total TGN46 protein levels were somewhat reduced in patient fibroblasts (Supplementary Fig. 11h).
245 These findings suggest that loss of Stx5S results in reduced COPI trafficking between GM130-marked cis- and
246 TGN46-marked trans-Golgi compartments.
247 Using an antibody specific to Stx5L (antibody specificity validated in Supplementary Fig. 13), we next
248 investigated whether the loss of Stx5S affects the intracellular distribution of Stx5L. An altered cellular
249 localization of Stx5L might imply a compensatory mechanism. Indeed, in Stx5M55V, Stx5L localizes more to the
250 cis-Golgi as measured by increased colocalization with GM130 (Fig. 4d, e). A slight increase in ER localization as
251 measured by PDI colocalization was also observed (Fig. 4f, g). Taken together, the loss of Stx5S causes Stx5L to
252 relocalize more towards the cis-Golgi. A possible explanation for the increased ER localization is that Stx5L will
253 also recycle more to the ER due to its ER retention signal[13,18,20–22], and is thereby displaced from other
254 compartments such as trafficking intermediates and post-Golgi compartments.
255
256 ***Loss of Stx5S compromises ER-Golgi trafficking***
257 As COPI is involved in retrograde Golgi-ER transport[40], we investigated whether trafficking at this interface is
258 compromised in Stx5M55V fibroblasts by using the fungal metabolite Brefeldin A (BFA), which inhibits COPI
259 vesicle formation[41]. If loss of Stx5S results in reduced retrograde Golgi-ER transport, we expect reduced
260 relocalization of Golgi-resident proteins to ER upon BFA treatment. Indeed, redistribution of GALNT2 from the
261 Golgi to the ER was incomplete in patient fibroblasts treated for 6 or 15 mins with BFA (Fig. 5a-c,
262 Supplementary Fig. 14), supporting a role for Stx5S in retrograde COPI trafficking. In addition, washout of BFA
263 caused a more rapid localization of GALNT2 to the Golgi apparatus in Stx5M55V, likely due to its incomplete
264 redistribution to the ER (Fig. 5a, d, Supplementary Fig. 14a-c).
265 We investigated the role of Stx5L in Golgi trafficking further using temperature-synchronizable vesicular
266 stomatitis virus G protein (VSVG) fused to GFP[42] in patient fibroblasts. At 40°C, VSVG does not fold correctly
267 and the VSVG-GFP protein remains trapped in the ER. A temperature shift to 32°C enables the correct
268 refolding of VSVG resulting in the synchronized release of VSVG-GFP from the ER, transit through the Golgi
269 network, and finally delivery at the plasma membrane where it becomes accessible to antibody labeling.
270 VSVG-EGFP appears at a Golgi-like compartment in both control and Stx5M55V fibroblasts at 30 mins after
271 temperature shift from 40°C to 32°C (Supplementary Fig. 14d), but after 60 mins plasma membrane
272 localization of VSVG is strongly reduced in Stx5M55V fibroblasts (Fig. 5e-g). Taken together, these findings

273 show that Stx5L is sufficient for anterograde trafficking until the Golgi, but the loss of Stx5S significantly
274 impairs intra- and/or post-Golgi trafficking, likely by the decrease of Stx5S-mediated intra-Golgi trafficking.
275 To further delineate the role of Stx5L in retrograde Golgi-ER trafficking, we performed a BFA experiment in the
276 Stx5L-lacking HeLa cells. In these cells, BFA resulted in faster relocalization of GALNT2 to the ER compared to
277 parental HeLa (Supplementary Fig. 15a, b), indicating that Stx5S suffices for retrograde COPI trafficking and the
278 expression of Stx5L counteracts this process. Further investigation of anterograde ER-Golgi trafficking in Stx5ΔL
279 cells with H-89 washout (Supplementary Fig. 15c, d), the retention using selective hooks (RUSH) system for
280 synchronized ER-Golgi transport[43] (Supplementary Fig. 15e, f, Supplementary Movies 1, 2) and temperature-
281 synchronizable VSVG[42] (Supplementary Fig. 15g, h, Supplementary Movies 3, 4) revealed no phenotype
282 relating to the loss of Stx5L. Thus, these data suggest Stx5L has no necessary function in ER-Golgi trafficking as
283 Stx5S can compensate, while Stx5L can only partly compensate for the loss of Stx5S in retrograde Golgi-ER and
284 intra-Golgi transport.
285
286 ***The two isoforms of Stx5 differently engage in SNARE complexes***
287 Our results in patient fibroblasts indicate differential trafficking roles of the two Stx5 isoforms in ER-Golgi
288 trafficking. One possible explanation for this is that Stx5S and Stx5L have different trafficking rates between
289 the ER and the Golgi. To test this, we fused each Stx5 isoform to streptavidin-binding protein (SBP) and
290 mCitrine (Stx5L-SBP-mCitrine and Stx5S-SBP-mCitrine; Stx5L-SBP-mCitrine carries the M55V mutation to
291 suppress expression of Stx5S). Moreover, we generated a mutant form of Stx5L where the RKR ER-retrieval
292 motif was converted to 3x alanine (AAA) (Stx5LΔER-SBP-mCitrine)[18], to delineate the role of this motif in ER-
293 Golgi transport. The co-expression of these constructs with ER-localized streptavidin enabled the synchronized
294 release of the Stx5 fusion proteins from the ER using biotin, which is the so-called RUSH system[43]
295 (Supplementary Fig. 16a). Co-expressing each Stx5 isoform with the Golgi marker Giantin fused to mScarlet[44] in
296 HeLa cells, allowed to visualize the trafficking of Stx5-SBP-mCitrine to the Golgi following the addition of biotin
297 (Supplementary Fig. 16a, b, Supplementary Movies 5-7). All three constructs were expressed at similar levels,
298 as judged from the fluorescent intensities. However, all Stx5 forms reached the Golgi with the same rate and
299 achieved maximal Golgi localization after about 20 minutes (Supplementary Fig. 16c-d. We also did not
300 observe any differences in the exit of the two isoforms from the Golgi (Supplementary Fig. 16c, e). This
301 suggests that the two isoforms traffic with similar rates between the ER and Golgi and that this is not

302 dependent on the RKR ER-retrieval motif of Stx5L. The altered morphologies of the ER and Golgi and the
303 compromised ER-Golgi trafficking are thus not caused by different trafficking rates of the two Stx5 isoforms.
304 Another explanation for the different trafficking roles of the two Stx5 isoforms is that they differently engage
305 in SNARE complexes. Since interactions of Stx5 with Bet1 and Bet1L mediate anterograde ER-Golgi transport
306 and retrograde intra-Golgi transport, respectively[2–5], we hypothesized that Stx5S would interact more strongly
307 with Bet1L. To test this, we developed an approach to visualize SNARE complexes based on a combination of
308 the RUSH system[43] and our previously developed FRET-FLIM approach for visualization of SNARE complexes[45]
309 (Fig. 6a). This FRET-FLIM approach employed Stx5 isoforms C-terminally fused with a donor fluorophore
310 (mCitrine) and Bet1L C-terminally fused with an acceptor fluorophore (mCherry). The formation of a post-
311 fusion SNARE complex results in the close proximity of the donor and an acceptor fluorophore resulting in
312 FRET which can be measured from a decreased donor fluorescence lifetime (τ). Contrary to ratiometric FRET,
313 FRET-FLIM is not dependent on local concentration differences or excitation intensities of the donor and
314 acceptor fluorophores, as τ is an intrinsic property of the fluorophore itself. By combining the FRET-FLIM
315 approach with the RUSH system, we were able to control the spatial localization of Stx5 isoforms and measure
316 interactions specifically at the ER (no biotin) or the Golgi apparatus (20 min after biotin addition; Fig. 6b-c). 30
317 minutes prior to imaging, cells were incubated with cycloheximide in culture medium to make sure
318 background interaction from any ER-localized newly-synthesized acceptor construct was mitigated.
319 For the mCitrine donor-only Stx5 constructs, we measured similar apparent fluorescence lifetimes for both
320 isoforms (Fig. 6c, Supplementary Fig. 17a, Stx5L: 2.92 ns ± 0.02, Stx5S: 2.92 ns ± 0.02 (mean ± 95%CI)) prior to
321 biotin addition, while these lifetimes slightly decreased following biotin addition (Fig. 6d, Supplementary Fig.
322 17a, Stx5L: 2.86 ns ± 0.03 , Stx5S: 2.85 ns ± 0.02 (mean ± 95%CI)). We attribute this reduced lifetime to the fact
323 that mCitrine is somewhat pH-sensitive[46] and the pH of the Golgi apparatus is lower than in the ER lumen[47].
324 We then co-expressed the Stx5 isoforms with mCherry-tagged Bet1L (Bet1L-mCherry) (Fig. 6a,b). At the ER,
325 thus before the release of Stx5 with biotin, we observed reduced average apparent fluorescence lifetimes for
326 both Stx5S and Stx5L with Bet1L-mCherry, compared to the donor-only controls (Fig. 6b, c, Stx5L: 2.48 ns ±
327 0.07, Stx5S: 2.49 ± 0.06 (mean ± 95%CI)), whereas the lifetimes of Stx5S and Stx5L did not significantly differ
328 from each other. After the release in the presence of biotin, this difference between Stx5L and Stx5S became
329 significant and average apparent fluorescence lifetimes were 2.33 ns (± 0.06 95%CI) for Stx5L while Stx5S
330 dropped to 2.24 ns (± 0.07 95%CI) (Fig. 6b, d). To validate that the observed effect is indeed caused by

331 functional SNARE complex formation, we repeated this experiment with VAMP8 instead of Bet1L as the
332 acceptor R-SNARE. VAMP8 has no role in ER-Golgi membrane fusion but rather associates with the late
333 endosomal/lysosomal compartment[33,45,48–52]. We only observed minor decreases in average apparent
334 fluorescence lifetimes for both Stx5L and Stx5S (Supplementary Fig. 17b, c, prior to biotin Stx5L: 2.83 ns ± 0.03,
335 Stx5S: 2.82 ± 0.03 (mean ± 95%CI), upon biotin addition Supplementary Fig. 17b, d, Stx5L: 2.78 ns ± 0.04, Stx5S:
336 2.76 ± 0.03 (mean ± 95%CI)). These FLIM results demonstrate that Stx5S interacts more strongly with Bet1L at
337 the Golgi than Stx5L. Thus, Stx5S is the dominant Qa-SNARE for intra-Golgi trafficking.
338
339 **Discussion**
340 Since the advent of the genomic age, close to 6,000 monogenic disorders have been discovered[53]. While nearly
341 all of these disorders result in a truncated, unstable and/or nonfunctional protein, e.g., due to a genetic
342 variant in the catalytic site or protein misfolding, isoform-specific mutations are rare. Here we identified a
343 mutation in an alternate site of ribosomal translation leading to human disease, namely the mutation of the
344 second starting methionine of Stx5. This mutation leads to the complete and specific loss of Stx5S. Although
345 *STX5* is an essential gene for embryonic development in mice[16,17], here we show that in humans the loss of
346 Stx5S still allowed a completed pregnancy. Nevertheless, patients have a very severe clinical pathology
347 characterized by infantile mortality due to liver disease, skeletal abnormalities and protein glycosylation
348 defects. While the exact mechanism for alternative translation is unclear, this might be an actively regulated
349 process. It could also be simply regulated by the affinity of the ribosome for the nucleotide sequence upstream
350 of the starting codon. Supporting the latter option, analysis of translation initiation sites with NetStart[54]
351 revealed that the starting codon of Stx5S is located in a more optimal nucleotide context than the starting
352 codon for Stx5L (Supplementary Fig. 18). This could lead to more leaky ribosomal scanning[55,56], resulting in the
353 more or less equimolar ratio of expression of Stx5L and Stx5S that we observed in fibroblasts and PBMCs of
354 healthy individuals. On the other hand, Western blot revealed different ratios of the two Stx5 isoforms in
355 different organs in rats[18], suggesting (i) that different cell types express different levels of Stx5S and Stx5L and
356 this is probably related to their exocytic function, and (ii) that the initiation of starting translation might be
357 regulated and not merely dependent on the binding affinities of the ribosome.
358 Cofractionation and microscopy studies have revealed that the localization of Stx5L and Stx5S overlap to a
359 large extent, but that they are generally distributed as a gradient between ER, ERGIC, and Golgi apparatus[20].

360 This observation has previously led to the suggestion that Stx5L might play a role in early Golgi trafficking,
361 while Stx5S functions in late Golgi trafficking[5,7,9–13,15,24,31]. Our data now shows that this is not the case and that
362 both Stx5 isoforms can mediate both early and late anterograde and retrograde Golgi trafficking with sufficient
363 fidelity to keep the layered Golgi morphology intact. However, the role of Stx5S is more important for
364 retrograde Golgi-ER and intra-Golgi trafficking, and its absence leads to an altered ER and Golgi morphology,
365 and altered distributions of glycosylation enzymes and trafficking proteins. The cumulative effect of slight
366 mislocalization of all glycosyltransferases might well explain the observed hypoglycosylation in the Stx5M55V
367 patients. Indeed, recent modeling showed that the slight mislocalization of glycosyltransferases can result in
368 large differences in glycosylation patterns, because glycosylation is the result of the sequential addition and
369 removal of different sugar moieties at the various Golgi compartments[36].
370 The dominant role of Stx5S in retrograde Golgi-ER and intra-Golgi trafficking is corroborated by the
371 observation that cellular levels of Bet1L, with known roles in intra-Golgi trafficking, are lower in Stx5M55V
372 patient cells. Interestingly, genetic variants in conserved oligomeric Golgi (COG) tethering complex
373 components, which are also implicated in CDGs, also resulted in lower levels of Bet1L as well and this was
374 attributed to a mislocalization of Bet1L to the ER where it was degraded[57]. Possibly, a similar mechanism might
375 explain the reduction in Bet1L levels in Stx5M55V patients. Although the Stx5-Bet1L interaction has been
376 reported in several studies[14,40], our study now shows this interaction in situ using FLIM. This interaction is
377 localization dependent and occurs mostly when Stx5 is localized at the Golgi. Moreover, we observed stronger
378 interaction of Bet1L with Stx5S compared to Stx5L at the Golgi, which is likely the result of the differential
379 localization of both isoforms.
380 An important function of the Golgi apparatus is protein glycosylation[58]. Collectively, somatic mutations
381 affecting glycosylation are classified as CDGs and currently over 100 monogenic diseases affecting
382 glycosylation have been identified[59,60]. A significant number of these include defects in Golgi trafficking, such
383 as the components of the conserved oligomeric Golgi tethering complex (COG)[37,61–68], mutations in genes
384 coding for the vacuolar H^+-ATPase and its assembly factors[69–72], and novel genes involved in Golgi ion
385 homeostasis[73–75]. Furthermore, defects are known in components associated with COPI-coated vesicles[76] that
386 result in deficient protein glycosylation in patient cells, but are not linked to abnormal glycosylation of proteins
387 in plasma and thus escape routine CDG screening. Our study revealed that mutations in ER-Golgi SNAREs can

388 also lead to CDG, thus highlighting the potential of glycosylation screening in patients to uncover novel cell
389 biological mechanisms.
390 While the cellular effects of the loss of Stx5S in Stx5M55V mutant fibroblasts are subtle, there can be
391 pronounced consequences in secretory cells, such as exocrine and endocrine cells, which are sensitive to
392 minor disruptions of the secretory pathway[58,76–78]. Not only can the defects in intra-Golgi trafficking explain the
393 hypoglycosylation in Stx5M55V patients, but also of other pathologies. For instance, Stx5 can participate in the
394 trafficking and processing of the very low-density lipoprotein receptor (VLDL-R) and this role is dependent on
395 the expression of Stx5[79], thus providing an explanation for the observed cholesterol homeostasis defect with
396 elevated cholesterol in all Stx5M55V patients.
397 In summary, we have demonstrated that a mutation in an alternative translation start site in Stx5 affects
398 intracellular membrane trafficking, leading to CDG. While there are previous descriptions of alternative start
399 site variations leading to disease[80], this study shows that mutations in an alternative starting codon causing the
400 loss of an isoform can also lead to disease.
401
402 **Acknowledgments**
403 We thank the family for participating in this study. We thank the following people for constructs: Hesso Farhan
404 and Franck Perez (Str-KDEL_ManII-SBP-EGFP; Addgene plasmid #65252), Jennifer Lippincott-Schwartz (pEGFP-
405 VSVG; Addgene plasmid #11912), Feng Zhang (pSpCas9n(BB)-2A-Puro (PX462) V2.0; Addgene plasmid #62987)
406 and Dorus Gadella (pmScarlet-i_Giantin_C1, Addgene plasmid #85050). We also thank the Microscopic
407 Imaging Center of the Radboud Institute for Molecular Life Sciences for use of their microscopy facilities.
408 N.H.R. is funded by a Long-Term Fellowship from the European Molecular Biology Organization (EMBO-LTF,
409 ALTF 232-2016) and a Veni grant from the Netherlands Organization for Scientific Research
410 (016.VENI.171.097). G.v.d.B. is funded by a Young Investigator Grant from the Human Frontier Science
411 Program (HFSP; RGY0080/2018) and a Vidi grant from the Netherlands Organisation for Scientific Research
412 (NWO-ALW VIDI 864.14.001). G.v.d.B has also received funding from the European Research Council (ERC)
413 under the European Union's Horizon 2020 research and innovation program (grant agreement No. 862137).
414 D.J.L. is funded by a Vidi grant (ZONMW VIDI 917.13.359), a ZONMW Medium Investment Grant (40-00506-98-
415 9001) from the Netherlands Organisation for Scientific Research, and Erare grants EUROCDG2 and

Euroglycanomics. K.Õ, M-A.V., S.P., and K.M. were supported by the Estonian Research Council grants GARLA8175, PUT355, PUTJD827 and PRG471.

Author Contributions

P.T.A.L., M.t.B., D.J.L., and G.v.d.B. designed the experiments and wrote the paper. E.C.F.G. contributed to the Stx5 kinetics, co-immunoprecipitation, and FLIM experiments. A.A., M.-A.V., M.B., F.Z., K.H., K.R., K.M., and K.Õ. contributed to the clinical data, exome sequencing and glycomics. O.F. and S.P. performed homozygosity mapping and prioritization of exome variants. N.H.R. and R.d.B. performed TEM. R.A. contributed to the Stx5ΔL experiments. P.T.A.L. and M.t.B. performed all other experiments. All authors contributed to writing the manuscript.

Competing Interests

The authors declare no competing interests.

Methods

Ethics

The study was approved by Research Ethics Committee of the University of Tartu (approval dates 19.12.2011, 20.02.2012 and 17.03.2014, and approval numbers 210/M-17, 212/M-31 and 235/M-13, 17.03.2014, respectively) and were strictly in accordance with the Declaration of Helsinki. Informed consent for carrying out research was obtained from the family of investigated individuals. Buffy coats and whole blood were obtained as anonymous coded specimens from the Dutch blood bank (Sanquin) and were handled according to known practice and legal guidelines. The research with human blood samples at the Department of Tumor Immunology complies with all institutional and national ethics regulations and has been approved by the ethics committee of Sanquin.

Glycosylation studies

Screening for CDG by isoelectric focusing (IEF) was carried out as before[70] as follows: for N-glycosylation screening, transferrin IEF was performed. 10 µL serum or plasma was added to a solution containing iron and $NaHCO_3$, electrophorized on a 5-7 pH gradient gel, and incubated with 60 µL polyclonal rabbit anti-transferrin

445 antibody (Dako, #A0061). Quantification of the gel was done with Image Quant software (TotalLab), by
446 expression of the intensity of the individual transferrin glycoforms as relative percentage of the total intensity
447 of transferrin bands. For mucin O-glycosylation screen, apolipoprotein CIII (apoCIII) IEF was performed. 2 µL of
448 serum or plasma was 15× diluted with saline solution. Before electrophoresis, the gel was rehydrated in a
449 solution containing 8 M urea. After blotting on a nitrocellulose membrane filter, the blot was washed and
450 blocked before incubation with anti-ApoC-III (1:2,000, Rockland, #600-101-114). After incubation with the
451 secondary anti-goat-HRP antibody (1:5,000, Thermo Scientific, #31402) and ECL reagent (Pierce), the blot was
452 visualized on a LAS3000 imaging system (Fujifilm). Blot quantification was done with Image Quant software by
453 expression of the intensity of the individual apoCIII glycoforms as relative percent of the total intensity of
454 apoCIII bands.
455 Plasma N-glycan profiling was performed by MALDI-TOF mass spectrometry of permethylated glycans[81], using
456 10 µL plasma. Glycans from 10 µL serum or plasma were cleaved with PNGaseF (NE Biolabs) and incubated
457 overnight. After purification on graphitized carbon SPE columns, the glycan were permethylated, purified
458 again, and eluted in 50 µL of 75% v/v aqueous acetonitrile. The glycans were dried and resuspended in a
459 methanol/sodium acetate mixture for spotting. Measurements were done on a AB SCIEX 5800 MALDI TOF/TOF
460 (Sciex). High resolution mass spectrometry of intact transferrin was performed on a 6540 nanochip QTOF
461 (Agilent), according to published protocols[82] as follows: 10 µL of serum or plasma sample was incubated with
462 anti-Tf beads before injection, and the eluate was analyzed on a microfluidic nanoLC-C8-chip 6540 QTOF
463 instrument (Agilent technologies). Agilent Mass Hunter Qualitative Analysis Software B.04.00 was used for
464 data analysis. For deconvolution of the charge distribution raw data, Agilent BioConfirm Software was used.
465
466 *Microarray analysis*
467 DNA was extracted either from peripheral blood according to the standard salting out protocol (IV:9 and IV:10)
468 or from amnionic fluid cell culture (IV:8). Screening for chromosomal abnormalities was performed using
469 HumanCytoSNP-12 BeadChips (Illumina Inc., San Diego, CA, USA). 200 ng of total DNA per sample was
470 processed according to the protocol supplied by the manufacturer. Genotypes were called by GenomeStudio
471 v2011.1 software and the data were analyzed using GenomeStudio Genome Viewer tool (Illumina Inc.). The
472 minimum threshold for LCSH (long contiguous stretches of homozygosity) regions was set at 5 Mb.
473

474 *Exome sequencing*

475 Genomic DNA was extracted from fibroblasts from patient IV:9 according to the manufacturer's protocol using
476 a Qiagen Mini Kit (Qiagen) and was checked for DNA degradation on agarose gels. Next generation sequencing
477 (NGS) and analysis were performed as described[71] as follows: exome enrichment was performed using the
478 SureSelect Human All Exon 50 Mb Kit (Agilent), covering ~21,000 genes. The exome library was sequenced on a
479 SOLiD 5500xl sequencer (Life Technologies). Color space reads were iteratively mapped to the hg19 reference
480 genome with the SOLiD LifeScope software version 2.1. Called variants and indels were annotated using an in-
481 house annotation pipeline[83,84] and common variants were filtered out based on a frequency of >0.5% in dbSNP
482 and a frequency of >0.3 % in our in-house database of >5,000 exomes. Quality criteria were applied to filter
483 out variants with less than 5 variant reads and less than 20% variation. Furthermore, synonymous variants,
484 deep intronic, intergenic and UTR variants were excluded. The identified variant was confirmed by Sanger
485 sequencing in all affected individuals (IV:8, IV:9, and IV:10) and their mother (III:2). Paternal DNA (III:1) was not
486 available.

487

488 *Cell culture*

489 HeLa cells (authenticated by ATCC through their human STR profiling cell authentication service), including
490 Stx5ΔL cell lines, were maintained in high glucose DMEM with Glutamax (Gibco 31966021). Human primary
491 dermal fibroblasts were obtained from patients or healthy donors and maintained in Medium 199 with EBSS
492 and L-glutamine (Lonza BE12-119F). All media were supplemented with 10% fetal calf serum (FCS, Greiner Bio-
493 one, Kremsmünster, Austria) and antibiotic-antimycotic solution (Gibco 15240-062). All cells were regularly
494 tested for mycoplasma contamination. Human peripheral blood mononuclear cells (PBMCs) were obtained
495 from buffy coats by Ficoll density centrifugation[85].

496

497 *Plasmids and transfection*

498 Str-KDEL_ManII-SBP-EGFP was a gift from Franck Perez (Addgene plasmid #65252). VAMP8-mCherry was
499 constructed earlier[45] and previously deposited to Addgene (Addgene plasmid #92424). Str-KDEL_Stx5L-SBP-
500 mCitrine and Str-KDEL_Stx5S-SBP-mCitrine were constructed by replacing the ManII-SBP-EGFP cassette in Str-
501 KDEL_ManII-SBP-EGFP using the AscI and XbaI restriction sites. Stx5 coding sequences were codon-optimized
502 for *Homo sapiens* using JCat and ordered from Genscript, the Stx5L coding sequence carries the M55V

503 mutation to suppress production of Stx5S. Stx5LΔER coding sequence was generated with Q5-polymerase site-
504 directed mutagenesis, using the Stx5L cDNA as a template with the following primer: 5'- CTTCG AATTC
505 AATGA TTCCG GCCGC CGCCT ACGGC AGCAA GAACA CC. Sequences were verified with Sanger
506 sequencing. HeLa cells were transfected with plasmid vectors using Fugene HD (Promega E2311), using the
507 recommended protocol of the manufacturer. Only cells expressing low to moderate levels of the transfected
508 plasmids, based on fluorescence intensity and manual localization scoring, were chosen for subsequent
509 microscopic analyses.
510
511 *CRISPR/Cas9*
512 Stable knock out of Stx5L in fibroblasts and HeLa cells was obtained using the CRISPR-CAS9 method. For this,
513 pairs of gRNA sequences were designed upstream of the *STX5* initiation codon (crispr.mit.edu, pair 1: ATAAC
514 CTCGG ACTGT TGTGG AGG and ATGAT CCCGC GGAAA CGCTA CGG; pair 2: TAACC TCGGA CTGTT GTGGA GGG
515 and TGATC CCGCG GAAAC GCTAC GGG). The gRNA sequences were cloned in pSpCas9n(BB)-2A-Puro (PX462)
516 V2.0 (gift from Feng Zhang, Addgene no. 62987)[86] and transfected into fibroblasts or HeLa cells by
517 electroporation (Neon Transfection System, Thermofisher, MA). After initial selection with puromycin, the
518 medium was changed for conditioned medium (collected from parental fibroblasts or wildtype HeLa cells at
519 70% confluency) supplemented 1:1 with fresh medium. Single clones were obtained and screened for
520 knockout of Stx5L by SDS-PAGE and Western blotting.
521
522 *Immunofluorescence*
523 Cells were plated on cleaned 12 mm glass coverslips (Electron Microscopy Services, 72230-01) and the
524 following day fixed with 4% paraformaldehyde for 15 minutes at room temperature. Following quenching with
525 50 mM NH_4Cl in PBS, cells were permeabilized and blocked in 2% normal donkey serum (Rockland, 017-000-
526 121) and 0.1% saponin (permeabilization buffer) for 30 mins at RT. Primary and secondary antibodies (list of
527 antibodies and dilutions in Supplementary Table 6) were diluted in permeabilization buffer and incubated for 1
528 hour at room temperature. Finally, cells were washed with 0.1% Triton X-100 in PBS to remove background
529 staining and mounted with mounting medium containing 0.01% Trolox (6-hydroxy-2,5,7,8-
530 tetramethylchroman-2-carboxylic acid) and 68% glycerol in 200 mM sodium phosphate buffer at pH 7.5 with

531 0.1 µg/ml DAPI. Coverslips were sealed with nail polish. Cells were imaged on a Leica SP8 SMD confocal laser
532 scanning microscope, equipped with an HC PL APO CS2 63x/1.20 WATER objective. Colocalization analysis was
533 performed using the *pearsonr* function from the Python package SciPy[87]. Individual cells were first saved to
534 separate .tiff files with ImageJ without any modifications, and then processed in a fully automated and
535 unbiased fashion using the *pearsonr* function.
536
537 *Lectin stainings*
538 Cells were plated on cleaned 12 mm glass coverslips for microscopy or 6-wells plates for flow cytometry and
539 after 72 hours culturing fixed with 4% paraformaldehyde. Cells were blocked with Carbo-Free Blocking solution
540 (Vector Laboratories, SP-5040) and incubated with 4 µg/mL biotinylated SNA-I (Vector Laboratories, B-1305) or
541 PNA (Vector Laboratories, B-1075) diluted in Carbo-Free Blocking solution. Cells were then incubated with
542 Streptavidin-Alexa Fluor 647 (ThermoScientific, S32357) before coverslips were mounted as described above.
543 Cells were imaged on a Leica SP8 SMD confocal laser scanning microscope, equipped with an HC PL APO CS2
544 63x/1.20 WATER objective. For flow cytometry, cells were resuspended in FACS buffer (phosphate buffered
545 saline + 0.5% FBS + 0.01% NaN_3). Flow cytometry samples were run on a FACSLyric flow cytometer (BD
546 Biosciences) and analyzed with FlowJo X (FlowJo, LLC).
547
548 *Brefeldin A assay*
549 Fibroblasts were plated in black clear-bottom 96-wells plates (Greiner, 655090) and cultured until 80%
550 confluent. Cells were either treated with 10 µg/mL Brefeldin A in DMSO (Cayman Chemicals, 11861) or DMSO
551 alone for 6 or 15 minutes in a humified incubator. Washout was performed by washing five times with
552 Leibovitz's L-15 (Gibco 21083027) with 10% FBS, then incubating in Leibovitz's L-15 with 10% FBS at 37°C for
553 the indicated times. After incubation, plates were transferred immediately to ice and cells were fixed with 4%
554 paraformaldehyde, after which the above immunofluorescence protocol was performed. Microscopy images
555 of the washout samples were acquired using a a Leica SP8 SMD confocal laser scanning microscope, equipped
556 with an HC PL APO CS2 63x/1.20 WATER objective. Microscopy images of the 15 minute incubation samples
557 were acquired using a Leica high-content microscopy system based on a Leica DMI6000B (Leica Microsystems)
558 and an HCX PL S-APO 40.0x0.75 DRY objective. HeLa cells were plated on 12 mm coverslips and incubated in
559 the same way with Brefeldin A, but fixed with 100% methanol at -20°C for 15 mins. Imaging of these samples

560 was performed using a Leica DMI6000B epifluorescence microscope equipped with an HC PL APO 63x1.40 OIL
561 objective. Cells were analyzed using Fiji (http://fiji.sc/) by first removing noise outliers (bright outliers, radius
562 2.0 pixels, threshold 50), then manually selecting cells and measuring the maximum fluorescence intensity in
563 these ROIs. Data were normalized to the mean of the DMSO control of each group.
564
565 *H-89 assay*
566 HeLa cells were plated on 12 mm coverslips and incubated the following day for 30 mins with 100 µM H-89
567 (Cayman Chemicals, 10010556) in DMSO or DMSO alone (vehicle) and H-89 was washed out with fresh
568 medium for 5 mins. Cells were fixed with 4% paraformaldehyde for 15 mins at RT and permeabilized with
569 100% methanol at -20°C for 15 mins prior to immunostaining with ERGIC53 mouse monoclonal antibody
570 (G1/93 or OTI1A8) before epifluorescence imaging as described for the BFA assay. Cells were analyzed using
571 Fiji and the number of ERGIC53-positive spots was quantified with the Spot Counter plugin. Data were
572 normalized to the mean fluorescence of the DMSO control of each group. Data was analyzed with a Mann-
573 Whitney U non-parametric test.
574
575 *Transmission electron microscopy*
576 Fibroblasts were grown in 12-wells plates and fixed with 2% glutaraldehyde (Sigma-Aldrich, G5882) in PB (0.1
577 M phosphate buffer, pH 7.4) for 60 mins at room temperature. Subsequently, cells were washed four times
578 with PB and post-fixed with 1% osmium tetroxide and 1% potassium ferrocyanide in PB for 60 mins at room
579 temperature. Then, cells were again washed four times with PB and four times with water. Cells were
580 incubated overnight in 0.5% uranyl acetate and dehydrated with graded steps of ethanol (30%, 50%, 70%,
581 96%, 100%) and embedded in Epon resin. 70 nm sections were stained with 2% uranyl acetate solution and
582 lead citrate solution. Stained sections were then examined using a CM12 transmission electron microscope
583 (Phillips).
584
585 *Live-cell epifluorescence microscopy*
586 Cells were seeded in four-compartment dishes (Greiner 627870) and transfected as described above (3:1
587 weight ratio reporter construct:Golgi label). Before imaging, the culture medium was exchanged for Leibovitz's
588 L-15 (Gibco 21083027). Samples were imaged using a DMI6000B (Leica Microsystems) with a heated stage

589 (Pecon) and objective heater. All samples were imaged using an HC PL APO 63x/1.40–0.60 OIL objective. VSVG-
590 ts045-EGFP experiments were performed at 32°C after overnight incubation at 40°C, while all other
591 epifluorescence experiments were performed at 37°C. For RUSH experiments, an equal amount of Leibovitz's
592 L-15 supplemented with biotin was added to the well immediately before imaging, to reach a final
593 concentration of 40 µM biotin. Live cell imaging was started immediately with 15 sec or 30 sec frame rates.
594 Analysis was performed with Fiji, after registration of the image stacks, the increase in fluorescence was
595 measured in the Golgi area by using the thresholded mScarlet-Giantin signal as an image mask.
596
597 *FRET-FLIM*
598 All imaging took place in Leibovitz's L-15 supplemented with 10 µg/mL cycloheximide (Sigma-Aldrich, C4859)
599 and cells were pulsed with biotin as described above. Imaging was performed on a Leica SP8 SMD system at
600 37°C, equipped with an HC PL APO CS2 63x/1.20 WATER objective. Fluorophores were excited with a pulsed
601 white light laser, operating at 80 MHz. mCitrine was excited at 514 nm, two separate HyD detectors were used
602 to collect photons, set at 521-565 nm and 613-668 nm respectively. Photons were collected for one minute
603 and lifetime histograms of the donor fluorophore were fitted with monoexponential decay functions
604 convoluted with the microscope instrument response function in Leica LAS X.
605
606 *SDS-PAGE and immunoblotting*
607 Cells were plated in 12-wells plates in culture medium and lysed the following day with SDS lysis buffer (1%
608 SDS, 10 mM Tris-HCl pH 6.8). Lysates were diluted to equal protein content (30 µg per lane) with SDS lysis
609 buffer, separated with SDS-PAGE on 4–20% Mini-PROTEAN TGX Precast Protein Gels (Biorad, 4561094) and
610 subsequently transferred onto 0.45 µm PVDF membranes. Small molecular weight proteins (Bet1 and Bet1L)
611 were separated on 16% Schaegger gels[88].
612
613 *Quantification and statistical analysis*
614 All mean values represent the average of all cells analyzed. All comparisons between two groups were first
615 checked for similar mean and median values and acceptable (< 3x) difference in variance, before statistical
616 analysis with an unpaired two-sided Student's t-test. Relative intensity data was first transformed using the
617 binary logarithm before analysis with an unpaired two-sided Student's t-test. H-89 data was analyzed with a

618 Mann-Whitney U non-parametric test. Brefeldin A washout data were analysed with an unpaired two-sided
619 Student's t-test between healthy donors and Stx5M55V patients followed by Bonferroni correction for
620 multiple comparisons. Stx5 kinetics data were analyzed with a one-way ANOVA, followed by a post-hoc
621 Tukey's honestly significant difference test. FRET-FLIM data were averaged per experiment before analysis
622 with a paired Student's t-test. $p < 0.05$ was considered significant. *$p < 0.05$, **$p < 0.01$, ***$p < 0.001$, ****$p \leq$
623 0.0001. All statistical analyses were performed using R statistical software. All numerical data were visualized
624 using R package *ggplot2*[89], with violins representing the overall distribution of the data and means ± 95% CI
625 overlaid.
626
627 *Data availability*
628 Source data are provided with this paper. The primary microscopy data generated in this study have been
629 deposited in the Zenodo database under accession code 10.5281/zenodo.5440334
630 (https://doi.org/10.5281/zenodo.5440334). The microarray and exome sequencing data are available under
631 restricted access for patient privacy reasons; access can be obtained upon request. The processed microscopy
632 data and complete Western blots generated in this study are provided in the Source Data file.
633
634 *Code availability*
635 ImageJ macros for quantification of the RUSH experiments are available upon request.

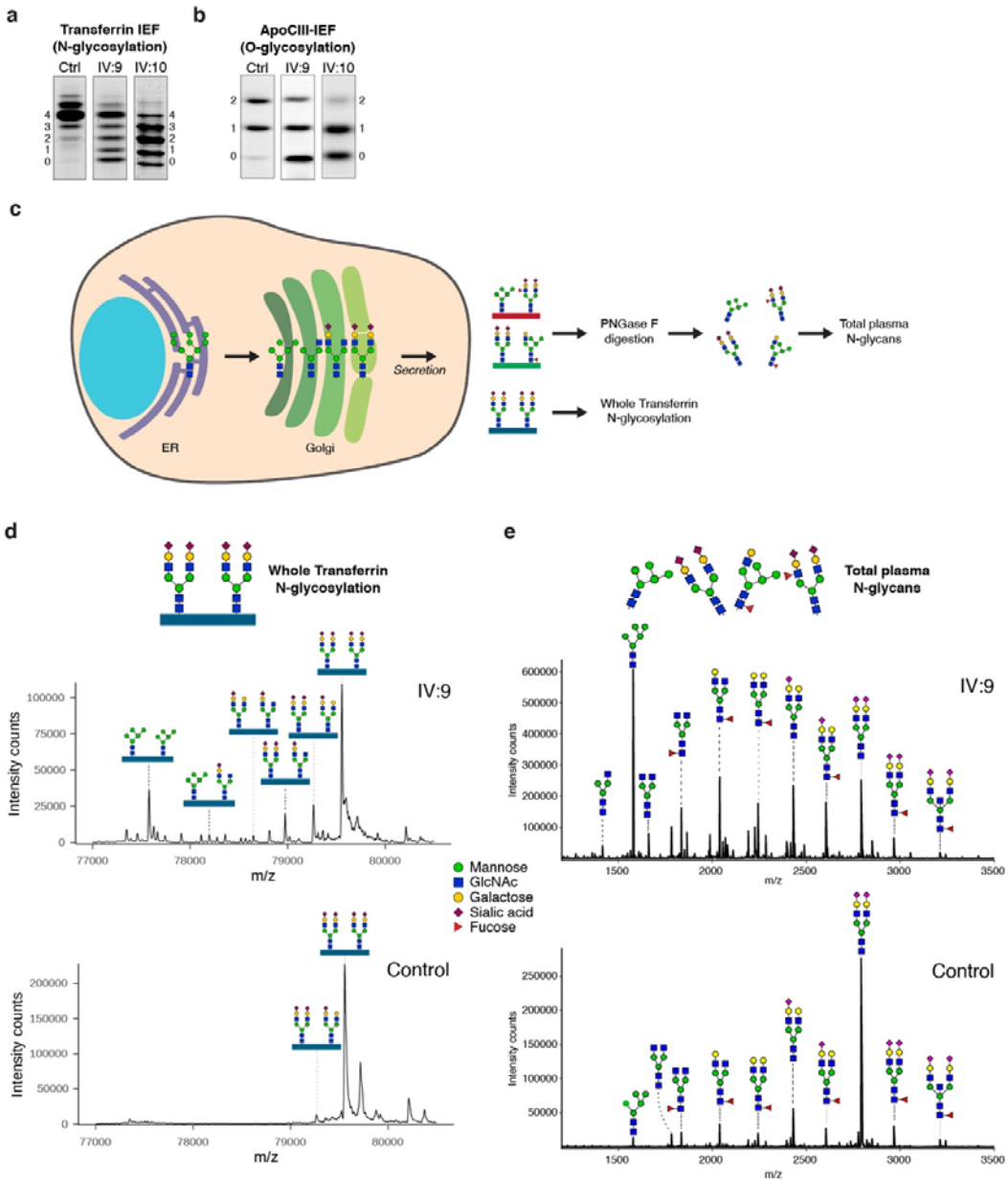

Figures

Figure 1. A novel, lethal, genetic variant suggests a defect in protein glycosylation related to Golgi trafficking.

(a) Glycosylation screening by isoelectric focusing (IEF) of serum transferrin. The accompanying numbers represent the total number of sialic acids in the different proteoforms. Both patients show a reduction in the number of sialic acids. Quantification of bands is shown in Supplementary Table 2.

642 (b) Glycosylation screening by IEF of serum Apolipoprotein C3 (ApoCIII). ApoCIII has one mucin-type O-linked
643 glycan with one or two sialic acids in controls. Both patients show a reduction in the number of sialic acids.
644 Quantification of bands is shown in Supplementary Table 2.
645 (c) Schematic overview of N-glycosylation intermediates in the Golgi. For mass spectrometry analysis of glycan
646 structures, glycosylated transferrin was enriched from all secreted glycoproteins in human serum and
647 subjected to intact protein mass spectrometry. In parallel, a different serum sample was treated with PNGase
648 F to cleave and analyze N-glycans from all plasma proteins.
649 (d) Nanochip-C8 QTOF mass spectra of enriched intact serum Transferrin of Stx5M55V patient IV:9 (top
650 spectrum) and healthy control (lower spectrum). Key transferrin glycoforms are shown, indicating a strong
651 increase of high-mannose glycans and glycans lacking sialic acid and galactose. Annotation of all peaks of
652 patients IV:9 and IV:10 is shown in Supplementary Table 3.
653 (e) MALDI-TOF mass spectra of total plasma N-glycans of Stx5M55V patient IV:9 (top spectrum) and healthy
654 control (lower spectrum). Structural analysis shows a strong increase of high-mannose glycans and glycans
655 lacking sialic acid and galactose. Annotation of all peaks of patients IV:9 and IV:10 is shown in Supplementary
656 Table 4.
657

658

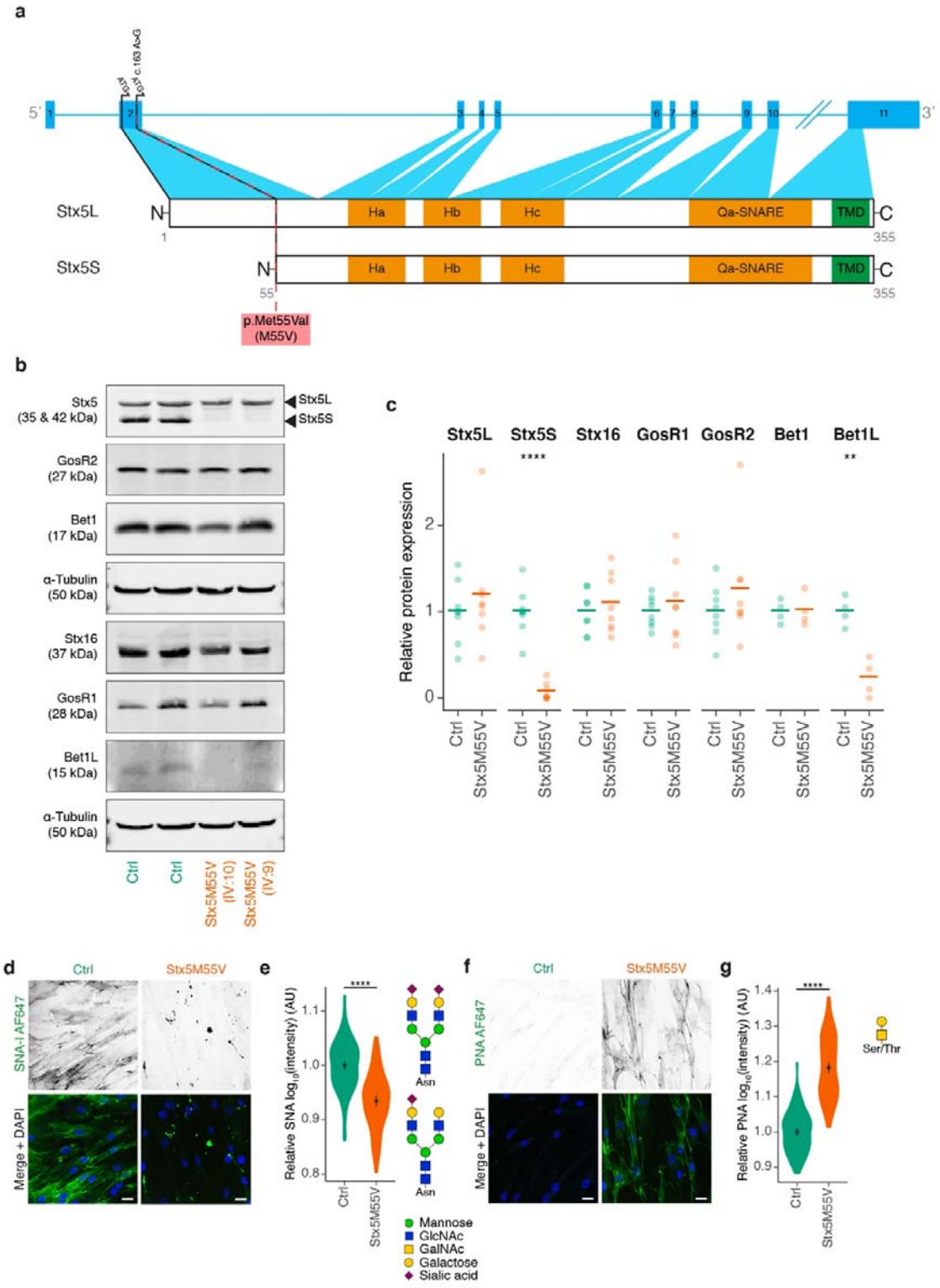
a
5'
3'
Stx5L
Stx5S
N
C
Ha
Hb
Hc
Qa-SNARE
TMD
1
355
55
p.Met55Val
(M55V)
b
Stx5
(35 & 42 kDa)
Stx5L
Stx5S
GosR2
(27 kDa)
Bet1
(17 kDa)
α-Tubulin
(50 kDa)
Stx16
(37 kDa)
GosR1
(28 kDa)
Bet1L
(15 kDa)
α-Tubulin
(50 kDa)
Ctrl
Ctrl
Stx5M55V
(IV:10)
Stx5M55V
(IV:9)
c
Stx5L
Stx5S
Stx16
GosR1
GosR2
Bet1
Bet1L
****
**
Relative protein expression
Ctrl
Stx5M55V
d
Ctrl
Stx5M55V
SNA-I AF647
Merge + DAPI
e
****
Relative SNA log10(intensity) (AU)
Asn
Asn
Mannose
GlcNAc
GalNAc
Galactose
Sialic acid
f
Ctrl
Stx5M55V
PNA AF647
Merge + DAPI
g
****
Relative PNA log10(intensity) (AU)
Ser/Thr

659

660 **Figure 2. Primary dermal fibroblasts are an accurate model of the glycosylation defect observed in**
661 **Stx5M55V patients.**

662 (a) Schematic representation of the intron-exon structure of *STX5* and the encoded proteoforms resulting from
663 the two starting codons in exon 2. The Stx5M55V genetic variant is indicated by a dashed red line. Orange
664 regions have a secondary helical structure. TMD, transmembrane domain. Ha, Hb, Hc: regulatory Habc-
665 domain.

666 (b) Immunoblot for SNARE proteins of cell lysates of primary human dermal fibroblasts from healthy donors
667 (green, Ctrl) or Stx5M55V patients (orange, Stx5M55V). Fibroblasts were obtained from two unique healthy
668 individuals and two patients. Lysates were loaded adjacent on single Western blots that were sequentially
669 probed for the mentioned proteins α-Tubulin loading control.

670 (c) Quantification of (b). Band intensities were first normalized to the loading control, then to the average
671 expression of both control lines. Each data point represents one cell line from two unique individuals tested at
672 least twice (average shown as bar). Unpaired two-sided Student's t-test; ****: $P = 1.1 \times 10^{-5}$; **: P = 0.0017;
673 other comparisons not significant.

674 (d) Fibroblasts of healthy donors (green, Ctrl) or Stx5M55V patients (orange, Stx5M55V) were probed with
675 SNA-I lectin (green in merge). Representative confocal micrographs. Scalebars, 25 µm. DAPI in blue.

676 (e) Quantification of (d). All data were $\log_{10}$-transformed and then normalized to the healthy donor. AU:
677 arbitrary units. N = 124 (Ctrl) and 111 (Stx5M55V) cells from two unique individuals tested twice. Mean ±
678 95%CI. Unpaired two-sided Student's t-test. ****: $P < 2.2 \times 10^{-16}$.

679 (f-g) Same as panels (d-e), but now for PNA lectin. N = 117 (Ctrl) and 122 (Stx5M55V) cells from two unique
680 individuals tested twice. Scalebars, 25 µm. Mean ± 95%CI. Unpaired two-sided Student's t-test. ****: $P < 2.2 \times$
681 10^{-16}.

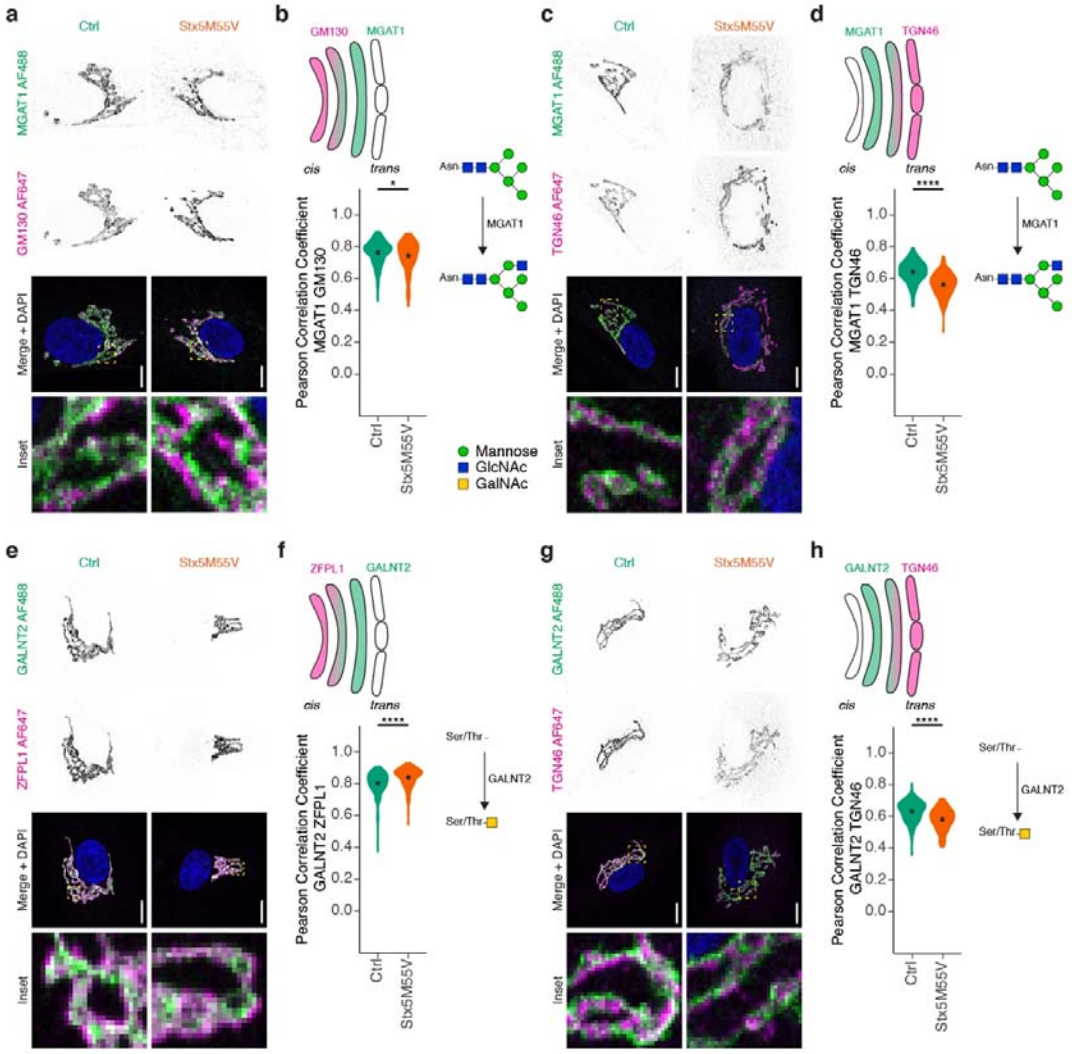

Figure 3. Glycosylation enzymes mislocalize in Stx5M55V patient fibroblasts.

(a) Immunofluorescence microscopy of MGAT1 (green in merge) and GM130 (magenta) in primary dermal fibroblasts of healthy donors (green, Ctrl) or Stx5M55V patients (orange, Stx5M55V). Representative confocal micrographs. Scalebars, 10 µm. DAPI in blue. N = 157 (Ctrl) and 126 (Stx5M55V) cells from two unique individuals tested twice.

(b) Pearson's correlations coefficients between MGAT1 and GM130 of panel (a). N = 157 (Ctrl) and 126 (Stx5M55V) from two unique individuals tested twice. Mean ± 95%CI. Unpaired two-sided Student's t-test. *: P = 0.047.

691 (c-d) Same as panels (a-b), but now for MGAT1 (green) and TGN46 (magenta). N = 157 (Ctrl) and 162
692 (Stx5M55V) cells from two unique individuals tested twice. Scalebars, 10 µm. Mean ± 95%CI. Unpaired two-
693 sided Student's t-test. ****: $P < 2.2 \times 10^{-16}$.

694 (e-f) Same as panels (a-b), but now for GALNT2 (green) and ZFPL1 (magenta). N = 240 (Ctrl) and 146
695 (Stx5M55V) cells from two unique individuals tested twice. Scalebars, 10 µm. Mean ± 95%CI. Unpaired two-
696 sided Student's t-test. ****: $P = 5.9 \times 10^{-7}$.

697 (g-h) Same as panels (a-b), but now for GALNT2 (green) and TGN46 (magenta). N = 172 (Ctrl) and 152
698 (Stx5M55V) cells from two unique individuals tested twice. Scalebars, 10 µm. Mean ± 95%CI. Unpaired two-
699 sided Student's t-test. ****: $P = 1.7 \times 10^{-11}$.

700

701
702

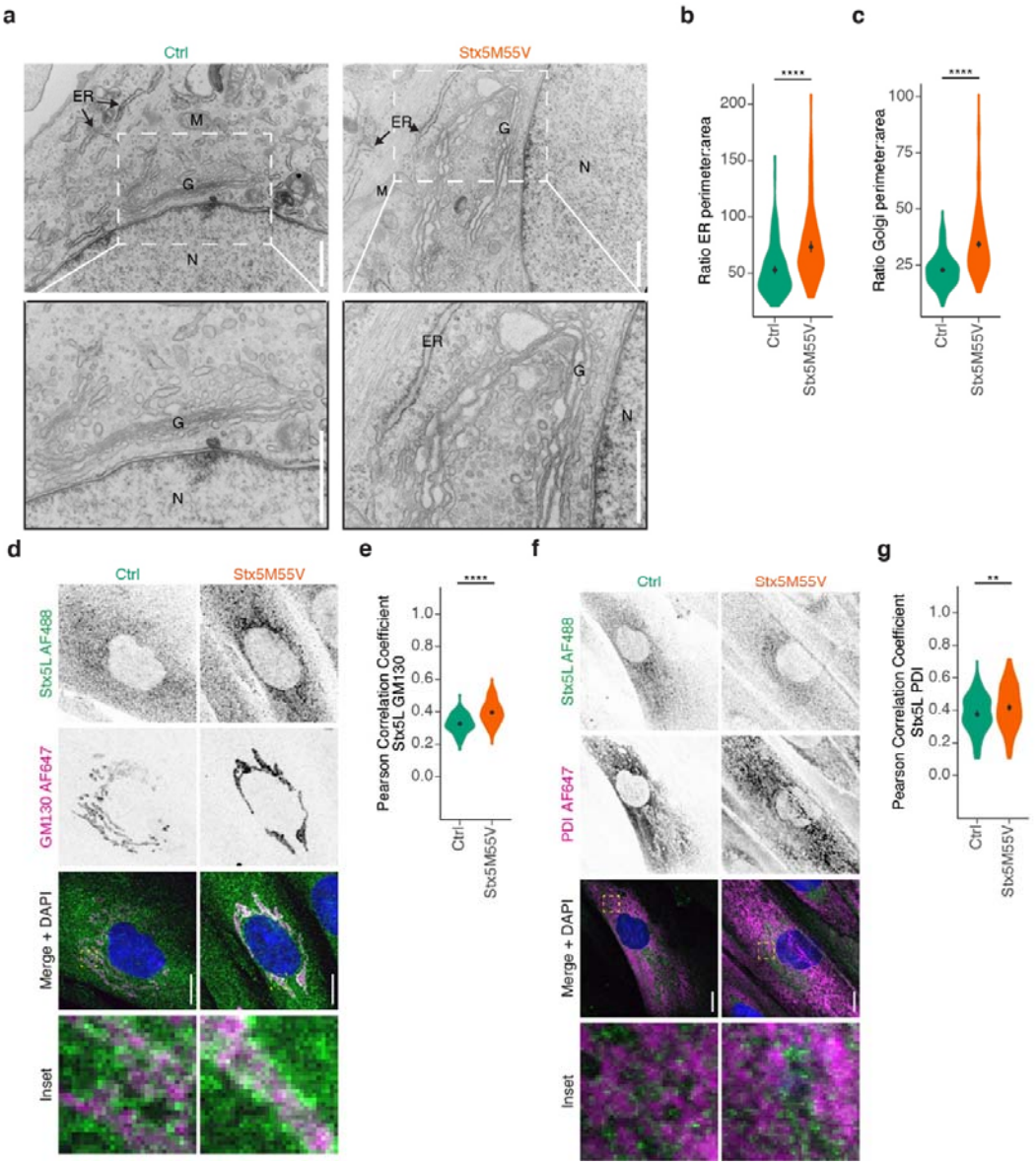

Figure 4. Loss of Stx5S alters ER and Golgi morphology.

(a) Representative transmission electron micrographs from healthy donor fibroblasts (left) or Stx5M55V patient fibroblasts (right). Scalebars, 1 µm. N, nucleus; G, Golgi apparatus; ER, endoplasmic reticulum; M, mitochondrion. More electron micrographs in Supplementary Fig. 9.

(b) ER perimeter and area quantification of panel (a), the ratios of the perimeters over the areas are plotted. N = 144 (both Ctrl and Stx5M55V) ER sections. Mean ± 95%CI. Unpaired two-sided Student's t-test. ****: $P = 3.8 \times 10^{-10}$.

(c) Same as panel (b), but now for Golgi. N = 400 (both Ctrl and Stx5M55V) Golgi sections. Mean ± 95%CI. Unpaired two-sided Student's t-test. ****: $P < 2.2 \times 10^{-16}$.

712 (d) Immunofluorescence microscopy of Stx5L (green in merge) and GM130 (magenta) in primary dermal
713 fibroblasts of healthy donors (green, Ctrl) or Stx5M55V patients (orange, Stx5M55V). Representative confocal
714 micrographs. Scalebars, 10 µm. DAPI in blue.

715 (e) Pearson's correlations coefficients between Stx5L and GM130 of panel (d). N = 102 (Ctrl) and 135
716 (Stx5M55V) cells from 2 unique individuals tested twice. Mean ± 95CI. Unpaired two-sided Student's t-test.
717 ****: $P = 9.45 \times 10^{-14}$.

718 (f-g) Same as panels (d-e), but now for Stx5L (green) and TGN46 (magenta). N = 147 (Ctrl) and 156 (Stx5M55V)
719 from 2 unique individuals tested twice. Scalebars, 10 µm. Mean ± 95CI. Unpaired two-sided Student's t-test.
720 **: P = 0.0051.

721

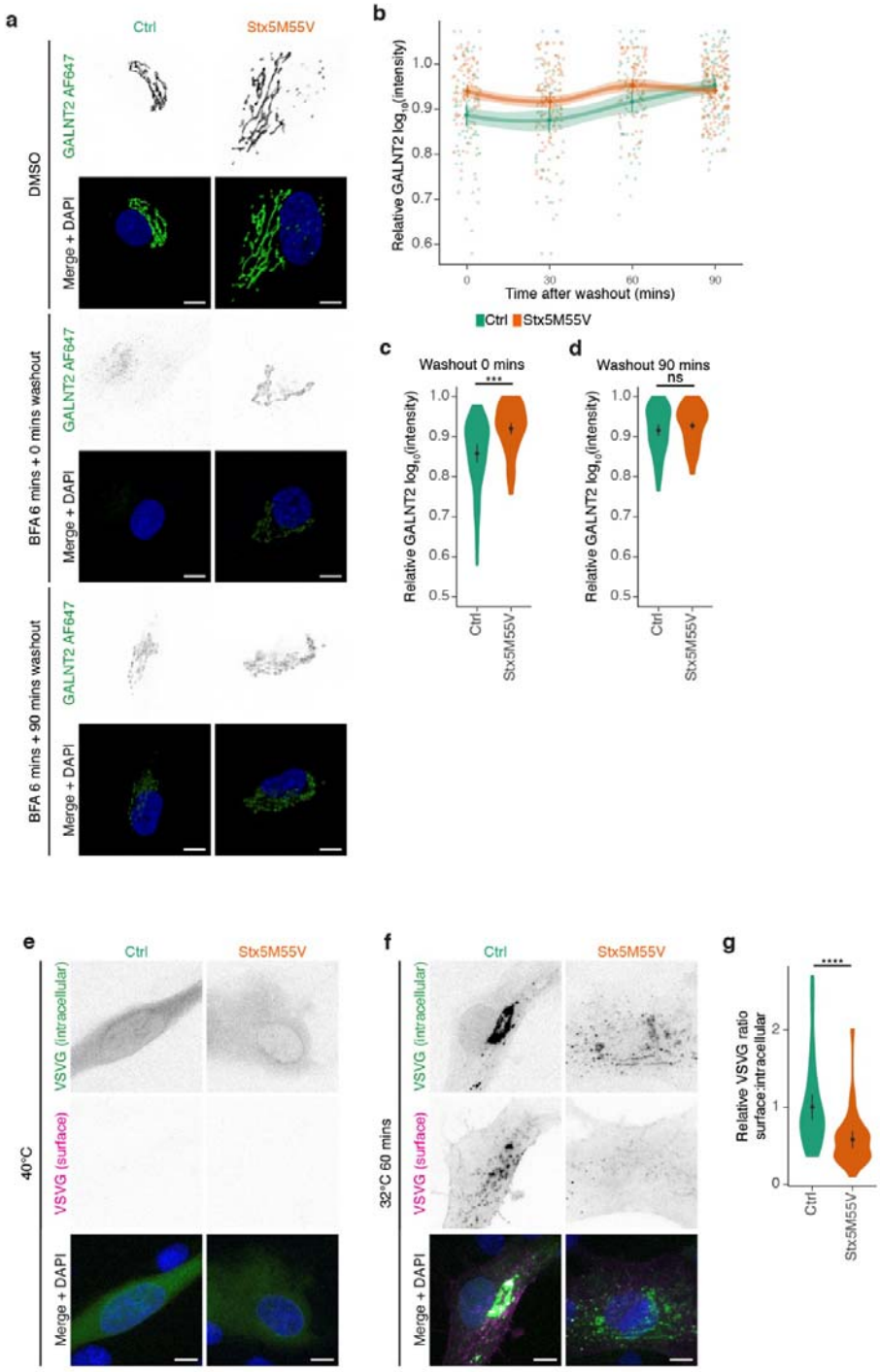

722
723 **Figure 5. Loss of Stx5S compromises ER-Golgi trafficking.**

724 (a) Immunofluorescence microscopy of GALNT2 (green in merge) in primary human dermal fibroblasts of
725 healthy donors (green, Ctrl) or Stx5M55V patients (orange, Stx5M55V) in the absence or presence of Brefeldin

726 A (BFA) for 6 min and washout for the indicated times. Representative confocal micrographs are shown.
727 Scalebars, 10 µm. DAPI in blue.
728 (b) Time course of relative maximum fluorescence intensities of GALNT2 from panel (a). All data were
729 normalized to the DMSO condition (vehicle). Mean ± 95%CI. Error bands are extrapolated 95%CI between the
730 timepoints.

731 (c) Quantification of the 0 min washout timepoint from panels (a) and (b). N = 76 (Ctrl) and 85 (Stx5M55V) cells
732 from two unique individuals tested twice. Mean ± 95CI. Unpaired two-sided Student's t-test, followed by
733 Bonferroni correction for multiple comparisons. ***: P = 0.00080.
734 (d) Same as (c), but now for the 90 min timepoint. N = 97 (Ctrl) and 152 (Stx5M55V) cells from two unique
735 individuals tested twice. Mean ± 95CI. Unpaired two-sided Student's t-test, followed by Bonferroni correction
736 for multiple comparisons; not significant.
737 (e) Immunofluorescence microscopy of VSVG-EGFP in primary human dermal fibroblasts of healthy donors
738 (green, Ctrl) or Stx5M55V patients (orange, Stx5M55V) cultured overnight at 40°C. Representative confocal
739 micrographs are shown. Scalebars, 10 µm. DAPI in blue.
740 (f) Same as (e), but now after 60 mins at 32°C. Scalebars, 10 µm.
741 (g) Quantification of the ratio of surface to intracellular of VSVG after 60 mins at 32°C. N = 45 (Ctrl) and 39
742 (Stx5M55V) cells from two unique individuals tested twice. Mean ± 95%CI. Unpaired two-sided Student's t-
743 test. ****: $P = 4.3 \times 10^{-5}$.
744

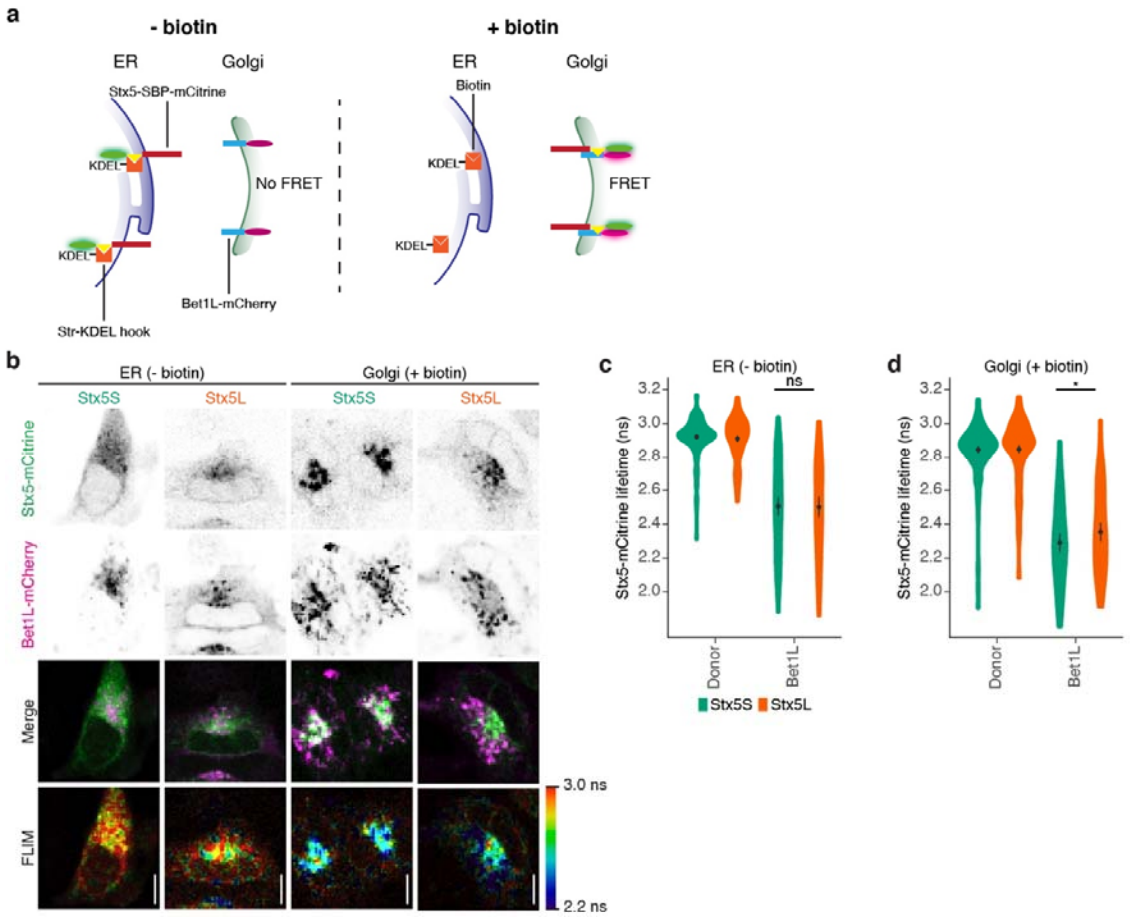

Figure 6. Stx5S is the dominant Qa-SNARE for intra-Golgi trafficking.

(a) Schematic overview of experimental design for complex formation of Stx5 isoforms with Bet1L, based on the RUSH system and SNARE complex measurement by FRET-FLIM. In absence of biotin (left panel), the reporter cargo (Stx5-SBP-mCitrine) is trapped at the ER by the lumenal Str-KDEL hook, and no FRET with Golgi-localized Bet1L-mCherry occurs. When biotin is added (right panel), biotin outcompetes the interaction with streptavidin, allowing Stx5-SBP-mCitrine to traffic freely to its destination compartment, and SNARE complex formation with Golgi-localized Bet1L-mCherry results in FRET. SBP, streptavidin binding protein; Str, streptavidin; FRET, Förster resonant energy transfer. FLIM, fluorescence lifetime imaging microscopy.

(b) Representative confocal micrographs and FLIM images of HeLa cells co-expressing Stx5-mCitrine (green in merge) and Bet1L-mCherry (magenta) without (ER) or with (Golgi) biotin. Scalebars, 10 µm.

(c-d) Stx5-mCitrine lifetimes at the ER (c) and Golgi (d) from panel (b). Donor: donor only control with cells only expressing Stx5S-SBP-mCitrine or Stx5L-SBP-mCitrine. N = 210 (Stx5S Donor ER), 202 (Stx5L Donor ER), 93 (Stx5S Bet1L ER), 83 (Stx5L Bet1L ER), 228 (Stx5S Donor Golgi), 228 (Stx5L Donor Golgi), 88 (Stx5S Bet1L Golgi)

759 and 88 (Stx5L Bet1L Golgi) cells from four to six independent experiments. Mean ± 95%CI. Paired two-sided
760 Student's t-test after taking the average for each experiment. ns: not significant; *: P = 0.012. Donor only
761 controls are not significant.

762 **References**

763 1. Jahn, R. & Scheller, R. H. SNAREs — engines for membrane fusion. *Nature Reviews*
764 *Molecular Cell Biology* **7**, 631–631 (2006).
765 2. Banfield, D. K., Lewis, M. J. & Pelham, H. R. B. A SNARE-like protein required for traffic
766 through the Golgi complex. *Nature* **375**, 806–809 (1995).
767 3. Parlati, F. *et al.* Topological restriction of SNARE-dependent membrane fusion. *Nature*
768 **407**, 194–198 (2000).
769 4. Parlati, F. *et al.* Distinct SNARE complexes mediating membrane fusion in Golgi transport
770 based on combinatorial specificity. *Proceedings of the National Academy of Sciences of*
771 *the United States of America* **99**, 5424–9 (2002).
772 5. Xu, Y., Martin, S., James, D. E. & Hong, W. GS15 Forms a SNARE Complex with Syntaxin
773 5, GS28, and Ykt6 and Is Implicated in Traffic in the Early Cisternae of the Golgi
774 Apparatus. *MBoC* **13**, 3493–3507 (2002).
775 6. Bentley, M. *et al.* SNARE status regulates tether recruitment and function in homotypic
776 COPII vesicle fusion. *The Journal of biological chemistry* **281**, 38825–33 (2006).
777 7. Dascher, C., Matteson, J. & Balch, W. E. Syntaxin 5 regulates endoplasmic reticulum to
778 Golgi transport. *The Journal of biological chemistry* **269**, 29363–6 (1994).
779 8. Rowe, T., Dascher, C., Bannykh, S., Plutner, H. & Balch, W. E. Role of vesicle-associated
780 syntaxin 5 in the assembly of pre-Golgi intermediates. *Science (New York, N.Y.)* **279**,
781 696–700 (1998).
782 9. Xu, D., Joglekar, A. P., Williams, A. L. & Hay, J. C. Subunit structure of a mammalian
783 ER/Golgi SNARE complex. *The Journal of biological chemistry* **275**, 39631–9 (2000).

784 10. Hay, J. C. *et al.* Localization, Dynamics, and Protein Interactions Reveal Distinct Roles for
785 ER and Golgi SNAREs. *The Journal of Cell Biology* **141**, 1489–1502 (1998).
786 11. Paek, I. *et al.* ERS-24, a Mammalian v-SNARE Implicated in Vesicle Traffic between the
787 ER and the Golgi. *The Journal of Cell Biology* **137**, 1017–1028 (1997).
788 12. Zhang, T. *et al.* Ykt6 forms a SNARE complex with syntaxin 5, GS28, and Bet1 and
789 participates in a late stage in endoplasmic reticulum-Golgi transport. *The Journal of*
790 *biological chemistry* **276**, 27480–7 (2001).
791 13. Linders, P. T., van der Horst, C., ter Beest, M. & van den Bogaart, G. Stx5-Mediated ER-
792 Golgi Transport in Mammals and Yeast. *Cells* **8**, 780 (2019).
793 14. Malsam, J. & Söllner, T. H. Organization of SNAREs within the Golgi stack. *Cold Spring*
794 *Harbor perspectives in biology* **3**, a005249–a005249 (2011).
795 15. Tai, G. *et al.* Participation of the Syntaxin 5/Ykt6/GS28/GS15 SNARE Complex in
796 Transport from the Early/Recycling Endosome to the Trans-Golgi Network. *MBoC* **15**,
797 4011–4022 (2004).
798 16. Dickinson, M. E. *et al.* High-throughput discovery of novel developmental phenotypes.
799 *Nature* **537**, 508–514 (2016).
800 17. Koscielny, G. *et al.* The International Mouse Phenotyping Consortium Web Portal, a
801 unified point of access for knockout mice and related phenotyping data. *Nucleic Acids*
802 *Res* **42**, D802–D809 (2014).
803 18. Hui, N. *et al.* An isoform of the Golgi t-SNARE, syntaxin 5, with an endoplasmic reticulum
804 retrieval signal. *Molecular biology of the cell* **8**, 1777–87 (1997).
805 19. Gao, G. & Banfield, D. K. Multiple features within the syntaxin Sed5p mediate its Golgi
806 localization. *Traffic* **21**, 274–296 (2020).

807 20. Dominguez, M. *et al.* gp25L/emp24/p24 protein family members of the cis-Golgi
808 network bind both COP I and II coatomer. *The Journal of cell biology* **140**, 751–65 (1998).
809 21. Miyazaki, K. *et al.* Contribution of the long form of syntaxin 5 to the organization of the
810 endoplasmic reticulum. *Journal of Cell Science* **125**, 5658 LP – 5666 (2012).
811 22. Suga, K., Saito, A., Tomiyama, T., Mori, H. & Akagawa, K. The Syntaxin 5 Isoforms Syx5
812 and Syx5L have Distinct Effects on the Processing of β-amyloid Precursor Protein. *The*
813 *Journal of Biochemistry* **146**, 905–915 (2009).
814 23. Avci, D. *et al.* The intramembrane protease SPP impacts morphology of the endoplasmic
815 reticulum by triggering degradation of morphogenic proteins. *J. Biol. Chem.* **294**, 2786–
816 2800 (2019).
817 24. Hay, J. C., Hirling, H. & Scheller, R. H. Mammalian vesicle trafficking proteins of the
818 endoplasmic reticulum and Golgi apparatus. *J. Biol. Chem.* **271**, 5671–5679 (1996).
819 25. Shestakova, A., Suvorova, E., Pavliv, O., Khaidakova, G. & Lupashin, V. Interaction of the
820 conserved oligomeric Golgi complex with t-SNARE Syntaxin5a/Sed5 enhances intra-Golgi
821 SNARE complex stability. *The Journal of Cell Biology* **179**, 1179–1192 (2007).
822 26. Linders, P. T. A., Peters, E., ter Beest, M., Lefeber, D. J. & van den Bogaart, G. Sugary
823 Logistics Gone Wrong: Membrane Trafficking and Congenital Disorders of Glycosylation.
824 *International Journal of Molecular Sciences* **21**, 4654 (2020).
825 27. Fung, C. W. *et al.* COG5-CDG with a Mild Neurohepatic Presentation. *JIMD Rep* **3**, 67–70
826 (2012).
827 28. Paesold-Burda, P. *et al.* Deficiency in COG5 causes a moderate form of congenital
828 disorders of glycosylation. *Hum. Mol. Genet.* **18**, 4350–4356 (2009).
829 29. Palmigiano, A. *et al.* MALDI-MS profiling of serum O-glycosylation and N-glycosylation in
830 COG5-CDG. *Journal of Mass Spectrometry* **52**, 372–377 (2017).

831 30. Rymen, D. *et al.* COG5-CDG: expanding the clinical spectrum. *Orphanet J Rare Dis* **7**, 94
832 (2012).
833 31. Zhang, T. *et al.* The Mammalian Protein (rbet1) Homologous to Yeast Bet1p Is Primarily
834 Associated with the Pre-Golgi Intermediate Compartment and Is Involved in Vesicular
835 Transport from the Endoplasmic Reticulum to the Golgi Apparatus. *The Journal of Cell*
836 *Biology* **139**, 1157–1168 (1997).
837 32. Mallard, F. *et al.* Early/recycling endosomes-to-TGN transport involves two SNARE
838 complexes and a Rab6 isoform. *The Journal of Cell Biology* **156**, 653–664 (2002).
839 33. Dingjan, I. *et al.* Endosomal and Phagosomal SNAREs. *Physiological Reviews* **98**, 1465–
840 1492 (2018).
841 34. Chiu, C.-F. *et al.* ZFPL1, a novel ring finger protein required for cis-Golgi integrity and
842 efficient ER-to-Golgi transport. *The EMBO journal* **27**, 934–47 (2008).
843 35. Gleeson, P. A. *et al.* p230 is associated with vesicles budding from the trans-Golgi
844 network. *Journal of Cell Science* **109**, 2811–2821 (1996).
845 36. Jaiman, A. & Thattai, M. Golgi compartments enable controlled biomolecular assembly
846 using promiscuous enzymes. *eLife* **9**, e49573 (2020).
847 37. Reynders, E. *et al.* Golgi function and dysfunction in the first COG4-deficient CDG type II
848 patient. *Hum Mol Genet* **18**, 3244–3256 (2009).
849 38. Climer, L. K., Pokrovskaya, I. D., Blackburn, J. B. & Lupashin, V. V. Membrane
850 detachment is not essential for COG complex function. *MBoC* **29**, 964–974 (2018).
851 39. Oka, T. *et al.* Genetic Analysis of the Subunit Organization and Function of the
852 Conserved Oligomeric Golgi (COG) Complex STUDIES OF COG5- AND COG7-DEFICIENT
853 MAMMALIAN CELLS. *J. Biol. Chem.* **280**, 32736–32745 (2005).

854 40. Glick, B. S. & Nakano, A. Membrane Traffic Within the Golgi Apparatus. *Annual Review*
855 *of Cell and Developmental Biology* **25**, 113–132 (2009).
856 41. Galea, G., Bexiga, M. G., Panarella, A., O'Neill, E. D. & Simpson, J. C. A high-content
857 screening microscopy approach to dissect the role of Rab proteins in Golgi-to-ER
858 retrograde trafficking. *J Cell Sci* **128**, 2339–2349 (2015).
859 42. Lippincott-Schwartz, J., Roberts, T. H. & Hirschberg, K. Secretory Protein Trafficking and
860 Organelle Dynamics in Living Cells. *Annual Review of Cell and Developmental Biology* **16**,
861 557–589 (2000).
862 43. Boncompain, G. *et al.* Synchronization of secretory protein traffic in populations of cells.
863 *Nature Methods* **9**, 493–493 (2012).
864 44. Bindels, D. S. *et al.* mScarlet: a bright monomeric red fluorescent protein for cellular
865 imaging. *Nature Methods* **14**, 53–56 (2017).
866 45. Verboogen, D. R. J., González Mancha, N., ter Beest, M. & van den Bogaart, G.
867 Fluorescence Lifetime Imaging Microscopy reveals rerouting of SNARE trafficking driving
868 dendritic cell activation. *eLife* **6**, (2017).
869 46. Griesbeck, O., Baird, G. S., Campbell, R. E., Zacharias, D. A. & Tsien, R. Y. Reducing the
870 Environmental Sensitivity of Yellow Fluorescent Protein MECHANISM AND
871 APPLICATIONS. *J. Biol. Chem.* **276**, 29188–29194 (2001).
872 47. Casey, J. R., Grinstein, S. & Orlowski, J. Sensors and regulators of intracellular pH. *Nature*
873 *reviews. Molecular cell biology* **11**, 50–61 (2010).
874 48. Antonin, W., Holroyd, C., Tikkanen, R., Höning, S. & Jahn, R. The R-SNARE
875 Endobrevin/VAMP-8 Mediates Homotypic Fusion of Early Endosomes and Late
876 Endosomes. *MBoC* **11**, 3289–3298 (2000).

877 49. Bajno, L. *et al.* Focal Exocytosis of Vamp3-Containing Vesicles at Sites of Phagosome
878 Formation. *J Cell Biol* **149**, 697–706 (2000).
879 50. Hong, W. SNAREs and traffic. *Biochimica et Biophysica Acta (BBA) - Molecular Cell*
880 *Research* **1744**, 120–144 (2005).
881 51. Manderson, A. P., Kay, J. G., Hammond, L. A., Brown, D. L. & Stow, J. L.
882 Subcompartments of the macrophage recycling endosome direct the differential
883 secretion of IL-6 and TNFα. *J Cell Biol* **178**, 57–69 (2007).
884 52. Murray, R. Z. A Role for the Phagosome in Cytokine Secretion. *Science* **310**, 1492–1495
885 (2005).
886 53. Amberger, J. S., Bocchini, C. A., Schiettecatte, F., Scott, A. F. & Hamosh, A. OMIM.org:
887 Online Mendelian Inheritance in Man (OMIM®), an online catalog of human genes and
888 genetic disorders. *Nucleic Acids Res* **43**, D789–D798 (2015).
889 54. Pedersen, A. G. & Nielsen, H. Neural network prediction of translation initiation sites in
890 eukaryotes: perspectives for EST and genome analysis. *Proc Int Conf Intell Syst Mol Biol*
891 **5**, 226–233 (1997).
892 55. Kochetov, A. V. Alternative translation start sites and hidden coding potential of
893 eukaryotic mRNAs. *BioEssays* **30**, 683–691 (2008).
894 56. Kozak, M. Regulation of translation via mRNA structure in prokaryotes and eukaryotes.
895 *Gene* **361**, 13–37 (2005).
896 57. Oka, T., Ungar, D., Hughson, F. M. & Krieger, M. The COG and COPI Complexes Interact
897 to Control the Abundance of GEARs, a Subset of Golgi Integral Membrane Proteins.
898 *MBoC* **15**, 2423–2435 (2004).
899 58. Ohtsubo, K. & Marth, J. D. Glycosylation in Cellular Mechanisms of Health and Disease.
900 *Cell* **126**, 855–867 (2006).

901 59. Freeze, H. H., Chong, J. X., Bamshad, M. J. & Ng, B. G. Solving Glycosylation Disorders:
902 Fundamental Approaches Reveal Complicated Pathways. *The American Journal of*
903 *Human Genetics* **94**, 161–175 (2014).
904 60. Fisher, P. & Ungar, D. Bridging the Gap between Glycosylation and Vesicle Traffic. *Front.*
905 *Cell Dev. Biol.* **4**, (2016).
906 61. Blackburn, J. B., Kudlyk, T., Pokrovskaya, I. & Lupashin, V. V. More than just sugars:
907 Conserved oligomeric Golgi complex deficiency causes glycosylation-independent
908 cellular defects. *Traffic* **19**, 463–480 (2018).
909 62. Foulquier, F. *et al.* Conserved oligomeric Golgi complex subunit 1 deficiency reveals a
910 previously uncharacterized congenital disorder of glycosylation type II. *PNAS* **103**, 3764–
911 3769 (2006).
912 63. Foulquier, F. *et al.* A new inborn error of glycosylation due to a Cog8 deficiency reveals a
913 critical role for the Cog1–Cog8 interaction in COG complex formation. *Hum Mol Genet*
914 **16**, 717–730 (2007).
915 64. Kranz, C. *et al.* COG8 deficiency causes new congenital disorder of glycosylation type IIh.
916 *Hum Mol Genet* **16**, 731–741 (2007).
917 65. Miller, V. J. & Ungar, D. Re'COG'nition at the Golgi. *Traffic* **13**, 891–897 (2012).
918 66. Morava, E. *et al.* A common mutation in the COG7 gene with a consistent phenotype
919 including microcephaly, adducted thumbs, growth retardation, VSD and episodes of
920 hyperthermia. *Eur J Hum Genet* **15**, 638–645 (2007).
921 67. Ng, B. G. *et al.* Molecular and clinical characterization of a Moroccan Cog7 deficient
922 patient. *Molecular Genetics and Metabolism* **91**, 201–204 (2007).
923 68. Wu, X. *et al.* Mutation of the COG complex subunit gene COG7 causes a lethal
924 congenital disorder. *Nat Med* **10**, 518–523 (2004).

925 69. Hucthagowder, V. *et al.* Loss-of-function mutations in ATP6V0A2 impair vesicular
926 trafficking, tropoelastin secretion and cell survival. *Hum Mol Genet* **18**, 2149–2165
927 (2009).
928 70. Jansen, J. C. *et al.* CCDC115 Deficiency Causes a Disorder of Golgi Homeostasis with
929 Abnormal Protein Glycosylation. *The American Journal of Human Genetics* **98**, 310–321
930 (2016).
931 71. Jansen, J. C. *et al.* TMEM199 Deficiency Is a Disorder of Golgi Homeostasis Characterized
932 by Elevated Aminotransferases, Alkaline Phosphatase, and Cholesterol and Abnormal
933 Glycosylation. *The American Journal of Human Genetics* **98**, 322–330 (2016).
934 72. Jansen, E. J. R. *et al.* ATP6AP1 deficiency causes an immunodeficiency with hepatopathy,
935 cognitive impairment and abnormal protein glycosylation. *Nature Communications* **7**,
936 11600–11600 (2016).
937 73. Foulquier, F. *et al.* TMEM165 Deficiency Causes a Congenital Disorder of Glycosylation.
938 *The American Journal of Human Genetics* **91**, 15–26 (2012).
939 74. Ashikov, A. *et al.* Integrating glycomics and genomics uncovers SLC10A7 as essential
940 factor for bone mineralization by regulating post-Golgi protein transport and
941 glycosylation. *Hum Mol Genet* **27**, 3029–3045 (2018).
942 75. Park, J. H. *et al.* SLC39A8 Deficiency: A Disorder of Manganese Transport and
943 Glycosylation. *The American Journal of Human Genetics* **97**, 894–903 (2015).
944 76. Witkos, T. M. *et al.* GORAB scaffolds COPI at the trans -Golgi for efficient enzyme
945 recycling and correct protein glycosylation. *Nat Commun* **10**, 1–18 (2019).
946 77. Zhong, W. Golgi during Development. *Cold Spring Harb Perspect Biol* **3**, (2011).
947 78. Zhao, H. Membrane Trafficking in Osteoblasts and Osteoclasts: New Avenues for
948 Understanding and Treating Skeletal Diseases. *Traffic* **13**, 1307–1314 (2012).

949 79. Wagner, T., Dieckmann, M., Jaeger, S., Weggen, S. & Pietrzik, C. U. Stx5 is a novel
950 interactor of VLDL-R to affect its intracellular trafficking and processing. *Experimental*
951 *Cell Research* **319**, 1956–1972 (2013).
952 80. Bogaert, A., Fernandez, E. & Gevaert, K. N-Terminal Proteoforms in Human Disease.
953 *Trends in Biochemical Sciences* **45**, 308–320 (2020).
954 81. Morelle, W. & Michalski, J.-C. Analysis of protein glycosylation by mass spectrometry.
955 *Nature Protocols* **2**, 1585–1602 (2007).
956 82. van Scherpenzeel, M., Steenbergen, G., Morava, E., Wevers, R. A. & Lefeber, D. J. High-
957 resolution mass spectrometry glycoprofiling of intact transferrin for diagnosis and
958 subtype identification in the congenital disorders of glycosylation. *Translational*
959 *Research* **166**, 639-649.e1 (2015).
960 83. Vissers, L. E. L. M. *et al.* A de novo paradigm for mental retardation. *Nature Genetics* **42**,
961 1109–1112 (2010).
962 84. Nikopoulos, K. *et al.* Next-Generation Sequencing of a 40 Mb Linkage Interval Reveals
963 TSPAN12 Mutations in Patients with Familial Exudative Vitreoretinopathy. *The American*
964 *Journal of Human Genetics* **86**, 240–247 (2010).
965 85. Jolanda, I., de Vries, M., Adema, G. J., Punt, C. J. A. & Figdor, C. G. Phenotypical and
966 Functional Characterization of Clinical-Grade Dendritic Cells. in *Adoptive*
967 *Immunotherapy: Methods and Protocols* (eds. Ludewig, B. & Hoffmann, M. W.) 113–125
968 (Humana Press, 2005). doi:10.1385/1-59259-862-5:113.
969 86. Ran, F. A. *et al.* Genome engineering using the CRISPR-Cas9 system. *Nature Protocols* **8**,
970 2281–2308 (2013).
971 87. Virtanen, P. *et al.* SciPy 1.0: fundamental algorithms for scientific computing in Python.
972 *Nature Methods* **17**, 261–272 (2020).

973 88. Schägger, H. Tricine–SDS-PAGE. *Nat Protoc* **1**, 16–22 (2006).

974 89. Wickham, H. *ggplot2: Elegant Graphics for Data Analysis*. (Springer-Verlag New York,

975 2016).

976

977